

# Two warm sub-Saturn mass planets identified from the TESS Full Frame Images<sup>★</sup>

Felipe I. Rojas<sup>1,2</sup>, Rafael Brahm<sup>3,2,4</sup>, Andrés Jordán,<sup>3,2,4</sup> Néstor Espinoza<sup>5</sup>, Thomas Henning<sup>6</sup>, Jan Eberhardt<sup>6</sup>, Melissa J. Hobson<sup>7</sup>, Martin Schlecker<sup>8</sup>, Marcelo Tala Pinto<sup>3</sup>, Trifon Trifonov<sup>6,9,10</sup>, Lyu Abe<sup>22</sup>, Gaspar Bakos<sup>11</sup>, Mauro Barbieri<sup>12</sup>, Khalid Barkaoui<sup>15,18,19</sup>, Christopher J. Burke<sup>13</sup>, R. Paul Butler<sup>14</sup>, Ilaria Carleo<sup>15,16</sup>, Karen A. Collins<sup>17</sup>, Jeffrey D. Crane<sup>23</sup>, Zoltan Csubry<sup>11</sup>, Phil Evans<sup>24</sup>, Tristan Guillot<sup>22</sup>, Chelsea X. Huang<sup>25</sup>, Jon M. Jenkins<sup>27</sup>, Matias Jones<sup>26</sup>, Diana Kossakowski<sup>6</sup>, David W. Latham<sup>17</sup>, Andrew W. Mann<sup>28</sup>, Djamel Mekarnia<sup>22</sup>, Maximiliano Moyano<sup>29</sup>, Sangeetha Nandakumar<sup>12</sup>, Hugh P. Osborn<sup>30</sup>, George Ricker<sup>13</sup>, David Rodriguez<sup>5</sup>, Paula Sarkis<sup>6</sup>, Richard P. Schwarz<sup>17</sup>, Sara Seager<sup>13,31,32</sup>, Ramotholo Sefako<sup>21</sup>, Stephen Shectman<sup>23</sup>, Gregor Srdic<sup>20</sup>, Stephanie Striegel<sup>33,27</sup>, Vincent Suc<sup>3,24</sup>, Johanna Teske<sup>18</sup>, Ian Thompson<sup>18</sup>, Pascal Torres-Miranda<sup>1,2</sup>, Roland Vanderspek<sup>13</sup>, José Vines<sup>29</sup>, Sharon X. Wang<sup>34</sup>, Joshua N. Winn<sup>11</sup>, and Carl Ziegler<sup>35</sup>

(Affiliations can be found after the references)

Received XXXX; accepted YYYY

## ABSTRACT

**Context.** Characterization of warm giants is crucial to constrain giant planet formation and evolution. Measuring the mass and radius of these planets, combined with their moderated irradiation, allows us to estimate their planetary bulk composition, which is a key quantity to comprehend giant planet formation and structure.

**Aims.** We present the discovery of two transiting warm giant planets orbiting solar-type stars from the Transiting Exoplanet Survey Satellite (TESS), which were characterized by further spectroscopic and photometric ground-based observations.

**Methods.** We performed a joint analysis of photometric data with radial velocities to confirm and characterize TOI-883b and TOI-899b, two sub-Saturns orbiting solar-like stars.

**Results.** TOI-883b and TOI-899b have masses of  $0.123 \pm 0.012 M_J$  and  $0.213 \pm 0.024 M_J$ , radius of  $0.604 \pm 0.028 R_J$  and  $0.991 \pm 0.044 R_J$ , periods of 10.06 d and 12.85 d and equilibrium temperature of  $1086 \pm 19 K$  and  $1040 \pm 19$ , respectively.

**Conclusions.** While having similar masses, orbital periods and stellar host properties, these planets seem to have different internal compositions, which could point to distinct formation histories. Both planets are suitable targets for atmospheric studies to further constrain formation scenarios of planets in the Neptune-Saturn mass range.

**Key words.** Planets and satellites: detection – Planets and satellites: gaseous planets – Techniques: photometric – Techniques: radial velocities

## 1. Introduction

The study of transiting planets having masses in the Neptune-Saturn range (sub-Saturns) is of particular interest in the context of giant planet formation because they can give us insights into some key processes involved in the core accretion scenario (Perri & Cameron 1974; Pollack et al. 1996; Mizuno 1980). Following this classical model, it is not easy to explain how these relatively heavy objects avoid triggering the runaway accretion of the surrounding gas to form massive gas giants (Rafikov 2006). More recent variations of the core accretion model that invoke the formation of giant planets through the accretion of icy pebbles (Lambrechts & Johansen 2012) allow for the formation of giant planets with large core-to-envelope mass ratios in the outer regions of the disk ( $\sim 25$  AU) but also closer to the water ice line (e.g. Bitsch et al. 2015). In this scenario, the more massive envelope-dominated gas giant planets are formed between these two regions. The measurement of the metallicity and composition of transiting sub-Saturns is key for identifying if these planets could have been formed in the regions predicted by these or other theoretical models (e.g. Mordasini et al. 2012).

Heavy element enrichment for transiting planets can be measured by comparing the measured planet masses and radii with predictions from structural models, which gives information about the bulk metallicity of the planet (e.g. Mordasini et al. 2012; Thorngren et al. 2016). It has also been proposed that the determination of the atmospheric enrichment of transiting giant planets can be used to constrain their formation conditions (e.g. Mordasini et al. 2016; Espinoza et al. 2017; Madhusudhan et al. 2017). In recent years, transiting sub-Saturns have attracted attention due to the detection of water features in their transmission spectra (e.g. Wakeford et al. 2018; Kreidberg et al. 2018; Colón et al. 2020), which is compatible with the formation of these planets in the ice-rich regions of the protoplanetary disk.

Despite the recent encouraging results for this population of transiting planets, one of the main limitations for using the current sample of well characterized (planet masses and radii measured with a precision of 20% or better) transiting sub-Saturns to infer properties about their structures and compositions through the modeling of their interiors, is that most of them orbit extremely close to their parent stars. The structure of the more massive sub-Saturns may be subject to the same unknown mechanism that inflates the radius of hot Jupiters (Laughlin et al. 2011), while on the low mass end, highly irradiated hot Neptunes are

<sup>★</sup> This paper includes data gathered with the 6.5 meter Magellan Telescopes located at Las Campanas Observatory, Chile

expected to lose a significant fraction of their envelopes through photo-evaporation (Owen & Lai 2018). Most of these short period sub-Saturns have been discovered with ground-based photometric surveys (e.g. Bakos et al. 2010, 2015; Pepper et al. 2017; Hellier et al. 2019) that lack the required duty cycle to efficiently detect giant planets with periods longer than 10 days. The NASA *Kepler* mission (Borucki et al. 2010) and its *K2* successor were responsible for finding the first dozen of transiting warm sub-Saturns whose masses were determined either from transiting timing variations (TTVs) of multiple systems (e.g. Holman et al. 2010; Panichi et al. 2018) and/or via radial velocity follow-up for those having brighter host stars (e.g. Barragán et al. 2016; Brady et al. 2018; Van Eylen et al. 2018; Brahm et al. 2019c). More recently, the TESS mission (Ricker et al. 2016) has started to efficiently detect transiting giant planet candidates with periods longer than 10 days, some of which have been found to have masses in the sub-Saturn regime (e.g. Huber et al. 2019; Addison et al. 2021; Dalba et al. 2020; Díaz et al. 2020).

In this study, we present the discovery of two new transiting warm giant planets with sub-Saturn masses that were first identified as candidates from the TESS Full Frame Images (FFIs). These planets were discovered in the context of the Warm gIaNTs with tEss (WINE) collaboration, which focuses on the systematic confirmation and orbital characterization of TESS transiting giant planets with orbital periods larger than 10 days (e.g. Brahm et al. 2019a; Jordán et al. 2020; Brahm et al. 2020; Schlecker et al. 2020; Hobson et al. 2021; Trifonov et al. 2021, 2023; Bozhilov et al. 2023; Brahm et al. 2023; Hobson et al. 2023; Eberhardt et al. 2023; Jones et al. 2024).

## 2. TESS data

### 2.1. TESS observations

TOI-883 was monitored by TESS from December 15, 2018, to January 6, 2019, in Sector 6 with a cadence of 30 minutes. It was subsequently observed in Sector 33 with a cadence of 2 minutes from December 18, 2020, to January 13, 2021.

On the other hand, TOI-899 was monitored by TESS in its 13 southern sectors, spanning a year of semi-continuous observations from July 25, 2018 to July 17, 2019. Besides having FFI data (30-minute cadence) for all these sectors, TOI-899 has 2-minute cadence observations for sectors 9-13, 29, 31, 33-37, 39, 61, 62, 64-66 and 68-69.

The image data were reduced and analyzed using the Science Processing Operations Center (SPOC) pipeline (Jenkins et al. 2016) at NASA Ames Research Center.

### 2.2. Tesseract pipeline

Both systems were detected on light curves extracted from the TESS FFIs. This was done using a pipeline developed by our team, called *tesseract*<sup>1</sup>.

*tesseract* has two ways to access data from the FFIs. The first one and used in this work depends on TESScut<sup>2</sup>, a service that runs *astrocut* (Brasseur et al. 2019) on the Mikulski Archive for Space Telescopes (MAST) servers, to download a cutout from TESS FFIs around the region of interest. The TESScut API is accessed through *astrocut* (Ginsburg et al. 2019). The second mode involves accessing a local file that contains

all the previously downloaded FFIs stacked together. The latter method was specially designed to generate large numbers of light curves, for example all bright targets ( $T_{\text{mag}} < 13$ ) from the TIC catalog. This avoids making an unreasonable number of calls to the TESScut service, reducing the time needed to generate a light curve.

The next subsections describe the steps taken after accessing the data through any previous methods.

#### 2.2.1. Postage Stamps

To obtain the light curve of a given target, the user can directly input the target's equatorial coordinates or the TIC ID. For the latter, its coordinates are resolved using *astrocut* (Ginsburg et al. 2019). If local files are used, then a call to *tess-point*<sup>3</sup> (Burke et al. 2020) is made to obtain the Camera and CCD where the target falls to select the right FFI stack.

Knowing the coordinates, the World Coordinate System (WCS) data is used to find the pixel coordinates of the target along the FFI and a postage stamp of  $21 \times 21$  pixels by default is created. This size is small enough to use a constant background estimation and at the same time, it gives a good number of pixels (441) to work with, considering that the aperture used for a 9th TESS Magnitude star tends to be between 6x6 (36) and 5x5 (25) pixels. Fainter targets are expected to cover an equal or smaller number of pixels. For this task, the *SEExtractorBackground* function from *photutils* (Bradley et al. 2019) is used. Very bright ( $T_{\text{mag}} < 9$ ), faint ( $T_{\text{mag}} > 14$ ) targets, crowded fields and nonstellar targets are examples where the user must exercise caution with the selected aperture and background behavior.

#### 2.2.2. Aperture photometry

By default, aperture selection on the cutouts follows the procedure of Lund et al. (2015). First, pixels above different flux thresholds are selected. These thresholds correspond to 1,3 and 5 times the median absolute deviation of the postage stamp flux. Over these groups, a Gaussian filter is applied and star masks are made employing the clustering algorithm DBSCAN (Ester et al. 1996) implemented in *scikit-learn* (Pedregosa et al. 2011). Finally, the watershed method, implemented in *scikit-image* (van der Walt et al. 2014), is applied to separate possible close targets on the same mask. The watershed method interprets the image as a topographic map and identifies boundaries associated with the watershed lines, as if water were flooding from the local minima. In this case, we simply use negative values of the flux in order to apply the method and select the sub-region that contains the already calculated pixel coordinate of the target.

Light curves are made for each aperture and stored in *lightkurve* (Lightkurve Collaboration et al. 2018) objects. These objects contain methods that allow us to flatten the light curves and calculate the Combined Differential Photometric Precision (CDPP) noise metric. The light curve with lower CDPP is selected.

The same procedure can be alternatively done using circular or custom apertures. These can be very useful in crowded fields and for targets near the saturation limit.

### 2.3. Transit search

An iterative transit search is made using Transit Least Squares (TLS; Hippke & Heller 2019) on all light curves for each sector.

<sup>1</sup> <https://github.com/astrofelipe/tesseract>

<sup>2</sup> <https://mast.stsci.edu/tesscut>

<sup>3</sup> <https://github.com/christopherburke/tess-point>

In particular, the TLS periodogram shows a significant signal of  $P \sim 10$  d in TOI-883 (Sector 6) and  $P \sim 12$  d in TOI-899, which can be found in all Sectors from 1 to 13. A visual inspection of the phased light curves reveals a transit signal in both targets (Figures 8 and 10). Then, all the in-transit points are masked and a new search is performed to search for additional transit signals. No additional signals were found. This procedure was also done using Box Least Squares (BLS; Kovács et al. 2002) obtaining similar results.

When these targets were classified as planet candidate hosts, neither of them were classified as TOIs and all the data had to be extracted from FFIs, except for TOI-899 in Sectors 9-13, proving the effectiveness of the pipeline.

#### 2.4. TOI status

The SPOC conducted a transit search with an adaptive, noise-compensating matched filter (Jenkins 2002; Jenkins et al. 2010, 2020), producing a threshold crossing event (TCE) for which an initial limb-darkened transit model was fitted (Li et al. 2019) and a suite of diagnostic tests were conducted to help make or break the planetary nature of the signal (Twicken et al. 2018). The TESS Science Office (TSO) reviewed the vetting information and issued an alert for TOI-883.01 and TOI-899 b on July 12, 2019 and July 15, 2019 (Guerrero et al. 2021) respectively. According to the difference image centroiding tests, the host star is located within  $0.84 \pm 2.5$  arcsec of the transit signal source of TOI-883 b and within  $0.16 \pm 2.7$  arcsec of the transit signal source of TOI-899 b. The Quick Look Pipeline (QLP; Huang et al. 2020a,b) also identified and vetted the candidates in July, 2019.

### 3. Ground-based follow-up

#### 3.1. Speckle imaging and Gaia sources

TOI-883 and TOI-899 were observed with the High-Resolution Camera (HRCam) installed at the 4.1m Southern Astrophysical Research (SOAR, Tokovinin 2018) telescope located on Cerro Pachón, Chile, on November 9 of 2019, as part of the SOAR TESS Survey (Ziegler et al. 2020). No nearby bright sources were identified for either target (Figure 1).

Additionally, with `tesseract` we generated plots including nearby Gaia (Gaia Collaboration et al. 2018) sources (up to  $G_{RP} = 17$ ), as seen in Figure 2. Both targets have companions, with TOI-883 in a more crowded field but surrounded mostly by faint targets, showing a minimum of  $\Delta T_{\text{mag}} \approx 5.65$  inside the aperture, at 20'', and TOI-899 with a minimum of  $\Delta T_{\text{mag}} \approx 2.65$  inside the aperture, at 32''.

Due to the TESS pixel scale (21''/pix), flux from nearby stars commonly falls inside the aperture used. To address this, we performed ground-based seeing-limited photometric follow-up observations with CHAT, El Sauce, LCOGT, and ASTEP to obtain a non-diluted transit depth, assuming the aperture is not contaminated by nearby sources. This is useful for estimating a dilution factor for TESS long cadence light curves, which will be used in the joint analysis. TESS short cadence light curves have been corrected for systematics, among other effects, including crowding, using the pipeline designed by the Science Processing Operations Center (SPOC). This correction is described in section 2.3.11 of Stumpe et al. (2012) and applied in the "PDCSAP" flux of these light curves.

#### 3.2. CHAT Photometry

TOI-883 was monitored over four separate nights using the 0.7-meter Chilean-Hungarian Automated Telescope (CHAT) located at Las Campanas Observatory. The observations were conducted in the Sloan *i* passband, utilizing an exposure duration of 16 seconds and a slight defocus.

Due to the limited constraints on the candidate ephemeris from the TESS observations, only one of the CHAT light curves was able to confirm the presence of the transit. These observations occurred on the night of December 20 of 2019 and detected an egress of TOI-883b during the first part of the observations.

TOI-899 was also observed with CHAT on March 27 of 2019. A full transit was obtained in the Sloan *i* passband. The adopted exposure time was 104 seconds and a mild defocus was applied which produced a typical peak flux of 15000 ADUs. Observations were interrupted for a couple of minutes after the ingress due to strong wind.

CHAT data for both targets were processed with a dedicated automated pipeline that was initially developed for data of the 1m LCOGT telescopes (Bayliss et al. 2015), and modified to produce light curves of CHAT in real time (e.g. Dorval et al. 2019; Zhou et al. 2019; Jones et al. 2019; Jordán et al. 2019; Hartman et al. 2019).

The transit obtained for TOI-883 is displayed in Figure 8 and for TOI-899 in Figure 10.

#### 3.3. El Sauce Photometry

TOI-899 was observed from the Evans 0.36 m telescope at El Sauce Observatory in Coquimbo Province, Chile. The telescope is equipped with a  $1536 \times 1024$  SBIG STT-1603-3 camera. The image scale is  $1''.47 \text{ pixel}^{-1}$ , resulting in an  $18.8' \times 12.5'$  field of view. Observations were made using a Rc filter on February 20, 2020, covering a full transit, which is shown in Figure 10. The photometric data were extracted using `AstroImageJ` (Collins et al. 2017) with circular  $8''.8$  photometric apertures, which exclude all flux from all known neighboring stars in the Gaia DR3 catalog.

#### 3.4. LCOGT

We used the Las Cumbres Observatory Global Telescope (LCOGT; Brown et al. 2013) 1.0 m network to observe both of our planet candidates. The 1.0 m network  $4096 \times 4096$  LCOGT SINISTRO cameras have an image scale of  $0''.389$  per pixel, resulting in a  $26' \times 26'$  field of view. The images were calibrated by the standard LCOGT BANZAI pipeline (McCully et al. 2018), and photometric data were extracted using `AstroImageJ`. TOI-883 was observed on December 14, 2021, in the Sloan zs band simultaneously from both the Cerro Tololo Inter-American Observatory (CTIO) LCOGT node and the McDonald Observatory (McD) node. A full transit and a gapped full transit were obtained, respectively. The photometric data were extracted using circular  $7''.8$  photometric apertures, which exclude all flux from all known neighboring stars in the Gaia DR3 catalog. The resulting lightcurves are shown in Figure 8. Full transits of TOI-899 were observed on February 5, 2021, simultaneously in B and Sloan zs bands from the South Africa Astronomical Observatory (SAAO) node near Sutherland, South Africa. The photometric data were extracted using circular  $5''.4$  photometric apertures, which exclude all flux from all known neighboring stars in the Gaia DR3 catalog. The resulting lightcurves are shown in Figure 10.

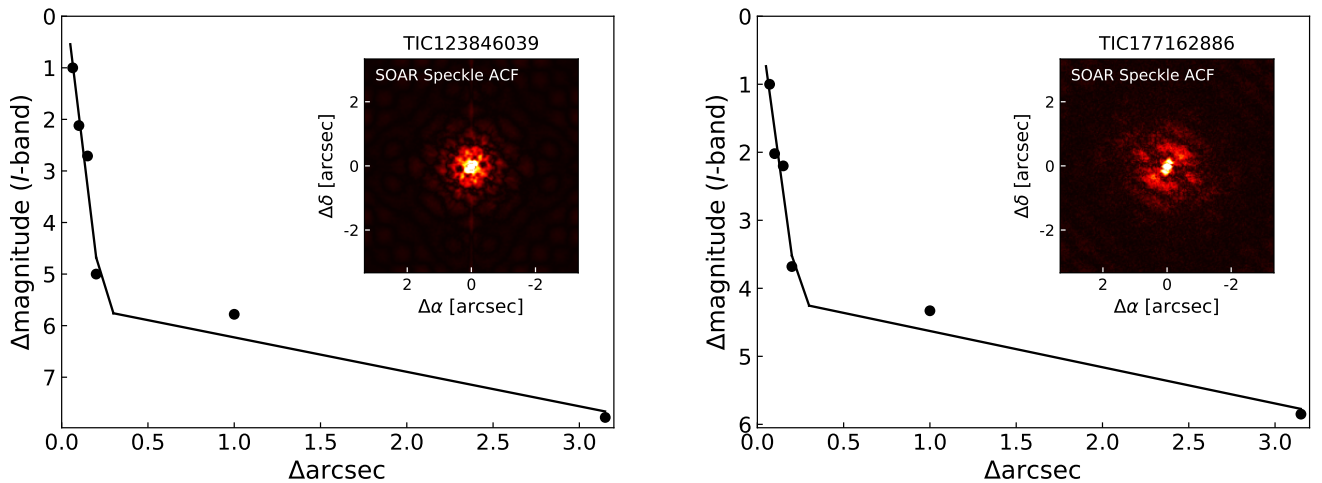


Fig. 1: Speckle images for TOI-883 and TOI-899 obtained with the Southern Astrophysical Research (SOAR). Both observations show no evidence for close companions.

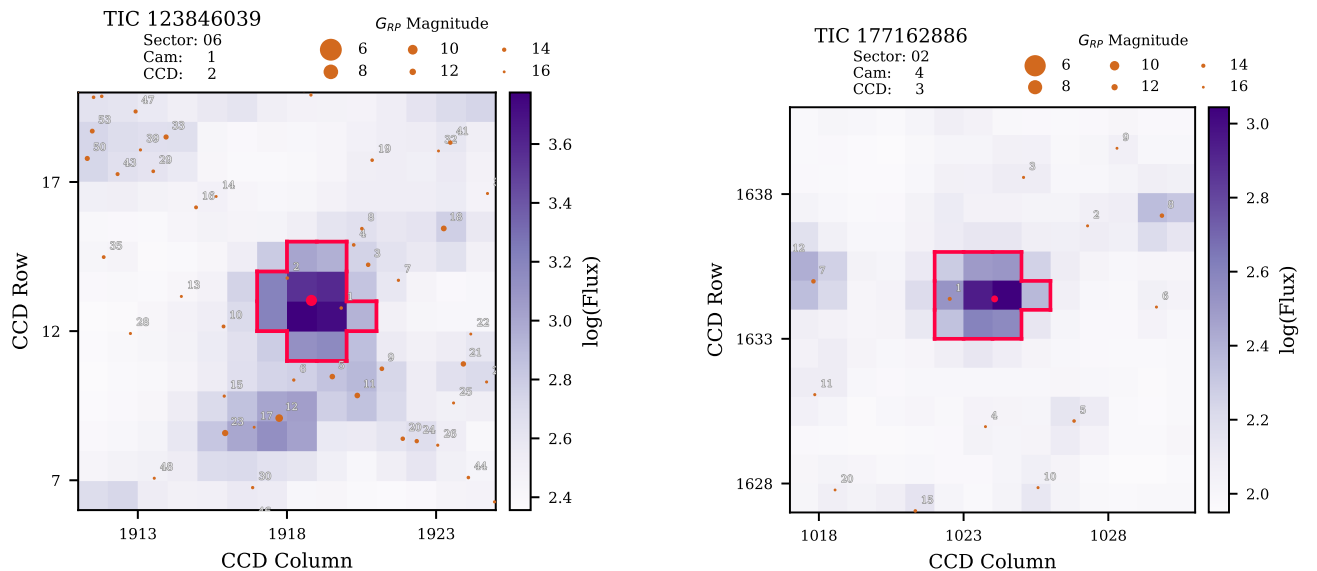


Fig. 2: Postage stamps for TOI-883 and TOI-899 (Sector 2), respectively, taken from the TESS FFIs. Orange dots correspond to nearby Gaia sources, with marker size proportional to their magnitude. Target location and aperture used to generate the light curve are plotted in red.

### 3.5. ASTEP

TOI-899 was observed with the Antarctica Search for Transiting ExoPlanets (ASTEP) telescope installed at Concordia station on the East Antarctic plateau (Guillot et al. 2015; Mékarnia et al. 2016).

The 0.4 m telescope was equipped with an FLI Proline science camera with a KAF-16801E,  $4096 \times 4096$  front-illuminated CCD with an image scale of  $0.93'' \text{ pixel}^{-1}$  resulting in a  $1 \text{ deg} \times \text{deg}$  corrected field of view. A dichroic plate was used to split the beam into a blue wavelength channel for guiding and a non-filtered red science channel roughly matching an Rc transmission curve (Abe et al. 2013). In January 2022, the focal box was replaced with a new one including two high sensitivity cameras for a two-colour (blue and red) simultaneous visible observations (Schmider et al. 2022).

The telescope is automated or remotely operated when needed. Due to the extremely low data transmission rate at the Concordia Station, the data are automatically processed on-site. The raw light curves are transferred to Europe on a server in Roma, Italy and are then available for deeper analysis.

Observations of TOI-899b were performed on 2020 June 6 and June 19. Weather conditions were good with a windless clear sky, and air temperatures ranging from  $-71^\circ\text{C}$  to  $-69^\circ\text{C}$  and from  $-77^\circ\text{C}$  to  $-73^\circ\text{C}$  on June 6 and June 19, respectively.

Full transits were observed on both 2020 June 6 and 19 observations with FWHMs of  $6''$  and  $5''$ , respectively. The Moon,  $\sim 99\%$  illuminated, was present during the 2020 June 6. The data were processed using IDL-based aperture photometry pipeline (Mékarnia et al. 2016). The light curves, shown in 10, were obtained with a circular  $11''$  photometric aperture.

### 3.6. High resolution spectroscopy

#### 3.6.1. FEROS

Both stars were initially monitored with the FEROS spectrograph (Kaufer et al. 1999) mounted on the MPG 2.2m telescope at La Silla Observatory.

TOI-883 was observed across 22 different epochs using FEROS from March 2019 to May 2019. An exposure time of 300 seconds was used, resulting in spectra with a signal-to-noise ratio (SNR) varying between 70 and 120, depending on the observing conditions and an average error on radial velocity of 6.65 m/s.

34 FEROS spectra of TOI-899 were obtained between March 2019 and May 2019. We adopted an exposure time of 1200 seconds, which translated into spectra with a typical SNR of 55 and an average error of 10.51 m/s on the radial velocity.

In both cases, observations were performed with the simultaneous calibration mode for tracing the instrumental radial velocity drift during the science exposure. The FEROS data were processed with the CERES pipeline (Brahm et al. 2017a). CERES performs the optimal extraction of the spectra, wavelength calibration, instrumental drift correction, and barycentric correction and computes the radial velocity and bisector span measurements by using the cross-correlation technique. In this case, a binary mask resembling the spectral lines of a G2-type star was used as the cross-correlation template. The obtained radial velocities are presented in Tables 7 and 8, for TOI-883 and TOI-899, respectively. In both cases, the RVs were consistent with low amplitude ( $K < 20 \text{ m s}^{-1}$ ) keplerian signal when adopting the TESS ephemeris, but the moderately large scatter around the best solution made evident the necessity of using more precise instruments to determine the mass of the planets.

#### 3.6.2. HARPS

We used the HARPS spectrograph (Mayor et al. 2003) mounted on the ESO 3.6m telescope at the ESO La Silla Observatory to further characterize the orbits of both transiting systems. For TOI-883, we obtained 14 HARPS spectra between April and December 2019. We used an exposure time of 900 s to reach a mean SNR of 80 and an average radial velocity error of 2.2 m/s. On the other hand, TOI-899 was observed on 9 different epochs with HARPS between December 2019 and February 2020, adopting an exposure time of 1800 s for reaching a typical SNR of 40 and a average radial velocity error of 5.1 m/s. The HARPS data was processed with the CERES pipeline to obtain precision radial velocities and bisector span measurements which are listed in Tables 7 and 8, and allowed us to confirm the planetary nature of both candidates and estimate the planetary masses.

#### 3.6.3. PFS

TOI-883 was monitored with the Planet Finder Spectrograph (PFS, Crane et al. 2006, 2008, 2010) mounted on the Magellan/Clay telescope at Las Campanas Observatory. 10 observations were made using the iodine cell with an exposure time of 1500 seconds. Each observation was performed between April and October 2019. An additional  $3 \times 1200$  s iodine-free template was obtained in December of 2019 to compute the radial velocities as explained in Butler et al. (1996), obtaining an average radial velocity error of 0.92 m/s. PFS radial velocities for TOI-883 are presented in Table 7.

#### 3.6.4. CHIRON

For TOI-899b, we acquired 6 epochs of observations with CHIRON spanning between November 2020 and January 2021, during the large program CARL-20B-3081 (PI: Carleo I.). CHIRON is a fiber fed high resolution echelle spectrograph on the SMARTS 1.5-meter telescope at Cerro Tololo Inter-American Observatory (CTIO) in Chile (Tokovinin et al. 2013). We used the fiber slicer mode, which allows a resolution of  $R \sim 80,000$  and a high efficiency (for details on different available observing modes with CHIRON, see e.g. Paredes et al. 2021), and spreads the spectrum into 59 orders.

We split each visit into three individual exposures to achieve better cosmic ray rejection and acquired long-exposed ThAr lamp spectra at the start and end of each visit to monitor the wavelength drift of the instrument. Since TOI-899b is a relatively faint target, we used an exposure time of 1200 seconds, reaching an average radial velocity error of 32 m/s.

The spectra were extracted by making use of the official spectral extraction pipeline of CHIRON as per Paredes et al. (2021). The radial velocities were calculated by a least-squares deconvolution of the observation against a synthetic non-rotating ATLAS9 model atmosphere spectrum (Castelli & Kurucz 2006). The least-squares deconvolution kernel is modeled via a broadening kernel encompassing the effects of radial velocity shift, rotational, instrumental, and macroturbulent broadening (Zhou et al. 2021). In addition, the RV pipeline allows matching the observed spectrum against an interpolated grid of  $\sim 10,000$  observed spectra pre-classified by the Spectroscopic Classification Pipeline (Buchhave et al. 2012) in order to estimate the spectral properties of the host star.

Radial velocities derived from CHIRON spectra are listed in Table 8.

## 4. Analysis

### 4.1. Stellar Parameters

We utilized the co-added FEROS spectra of each host star to determine their atmospheric parameters ( $T_{\text{eff}}$ ,  $\log g$ ,  $[\text{Fe}/\text{H}]$ ,  $v \sin i$ ) using the ZASPE code (Brahm et al. 2017b). This code analyzes the observed high-resolution spectrum by comparing it to a grid of synthetic models created from the ATLAS9 model atmospheres (Castelli & Kurucz 2004), focusing on spectral regions that are particularly sensitive to variations in the atmospheric parameters.

The physical parameters and evolutionary stages of the host stars are derived from the PARSEC (Bressan et al. 2012) stellar isochrones, along with the Gaia DR2 parallax, 2MASS (Cutri et al. 2003), Gaia broadband magnitudes and the atmospheric parameters obtained from ZASPE, as detailed in Brahm et al. (2019b). In summary, we identify the parameters of the PARSEC model that yield synthetic broadband photometric magnitudes that closely match the observed values while ensuring that the stellar effective temperature is compatible with that determined by ZASPE. We only consider PARSEC models with metallicities matching the spectroscopic values, and we convert the absolute magnitudes from these models into apparent magnitudes using the parallax and the extinction laws from Cardelli et al. (1989), considering the extinction coefficient  $A_v$  as an additional free parameter. Through this method, we acquire the posterior parameters using the emcee package (Foreman-Mackey et al. 2013). This procedure yields the stellar mass and radius, allowing us to calculate a refined value for the stellar  $\log g$  that is more accurate

than the spectroscopic estimate obtained via ZASPE. Given the correlations involved in determining the spectroscopic parameters, we repeat the ZASPE analysis again, fixing  $\log g$  to this new value, and then we repeat the determination of the stellar physical parameters, iterating until convergence in  $\log g$  is achieved.

The final atmospheric and physical parameters for TOI-883 and TOI-899 are listed in Table 1. Both stars are G-type stars with very similar effective temperatures around 5700 K.

#### 4.2. Global Modelling

For both targets, we performed an analysis of the photometric and radial velocity data using `juliet` (Espinoza et al. 2018), which allows us to do joint fits for photometry, using the `batman` (Kreidberg 2015) package, and RVs, using the `radvel` (Fulton et al. 2018) package. The parameter inference is done using nested sampling via the `MultiNest` package (Feroz et al. 2009) through `PyMultiNest` (Buchner et al. 2014) packages or the `dynesty` package (Speagle 2020).

Nested sampling allows us to compute the log-evidences  $\ln Z$  from the Bayesian model, which can be used for model comparison. When a  $\Delta \ln Z > 3$  difference is present, the model with larger Bayesian log evidence is favored. If not, then both models are indistinguishable and the simpler model is chosen.

For the limb-darkening (LD) parametrization, we use a quadratic law for TESS light curves and a linear law for CHAT light curves. This selection was made following Espinoza & Jordán (2016). Both cases use the uninformative sampling scheme of Kipping (2013). Long integration times, such as TESS 30-min cadence, cause a smearing effect on light curves, biasing the parameters obtained with a model that assumes unbinned data. We follow the method of Kipping (2010) and choose to resample long cadence light curves to have an integration time comparable to the short cadence ones. This implies resampling the 30-minute cadence light curves by a factor of 20.

Rather than using the planet-to-star radius ratio  $p = R_p/R_*$  and the impact parameter  $b$ , the parametrization  $r_1$  and  $r_2$  was used, previously defined in (Espinoza 2018). These parameters ensure that all physically possible values in the (p,b) plane are explored.

Specific considerations for each system are described in section 4.4.

#### 4.3. Radial Velocities

We conducted a preliminary analysis using only radial velocities to identify additional non-transiting planets. We utilized the RVSearch pipeline (Rosenthal et al. 2021) to search iteratively for signals ranging from 1 day to the total observation baseline. Priors for period and time of conjunction for planet b, were established based on photometric data. The possibility of a linear trend was also explored. Only the transiting planets were recovered with sufficient significance for both targets. We independently validated this finding using an  $l_1$  periodogram (Hara et al. 2017), which analyzes all frequencies simultaneously, resulting in a cleaner power spectrum.

#### 4.4. Joint Analysis

For the two systems, we performed a joint analysis of all available photometry and radial velocity data (TESS and ground-based) to infer the corresponding orbital parameters. For the photometric model, we included a Gaussian Process (GP) to account

for underlying systematic or astrophysical signals present in the TESS long cadence data (see Figures 5 and 6). As this adds significant computation time and we only care about the transits, we used only data within a 3-day window centered on each transit. A Matern 3/2 kernel was chosen for the GP model, which is parametrized by  $\sigma_{GP}$  and  $\rho$  as follows:

$$k(\tau) = \sigma_{GP}^2 \left( 1 + \frac{\sqrt{3}\tau}{\rho} \right) \exp\left(-\frac{\sqrt{3}\tau}{\rho}\right)$$

Using information previously obtained via BLS and RV-only analysis, we use normal priors for the period  $P$ , time of transit center  $t_0$  and radial velocity offset  $\mu$ . The remaining parameters were explored using uniform or log-uniform priors, depending on whether the parameter space spanned several orders of magnitude. For non-eccentric models, eccentricity  $e$  was fixed to 0 and  $\omega$  to 90 degrees. A summary of all values used is listed in Table 2.

For TOI-899, each of the 23 sectors should ideally be considered as a different instrument. The reason behind this is that, for each sector, the target fell on different CCDs, cameras and pixels. In addition and as a consequence of the above, the pipeline makes different aperture choices (see Figure 4). Considering all this, even with fixed apertures, each light curve should exhibit different noise and instrumental systematics. However, this implies a large increase in the number of parameters, making the analysis computationally intensive. To address this, a photometric fit of each sector was performed and compared the noise related parameters. Short and long cadence sectors were grouped and used as independent instruments instead.

Evidence for both models is reported in Table 4, which favors a non-eccentric model for TOI-883b and eccentric model for TOI-899b. Inferred parameters for this model are reported in Table 5. The physical parameters of the systems are listed in Table 6. We follow the suggestions from Tayar et al. (2022), adding their error floors to the stellar parameters in quadrature.

#### 4.5. Transit Timing Variations of TOI-899b

Given that TOI-899 was observed in the 13 TESS sectors of the southern hemisphere, we searched for transit timing variations of TOI-899b that could be induced by additional planets in the system. We ran an independent `juliet` fit on the photometry, leaving the time of transit as a free parameter and using all the transit data available: 13 from TESS in long cadence, 26 from TESS in short cadence, plus 2 from the follow-up data acquired with CHAT and El Sauce. We adopted normal priors using the results from Table 5. The difference between observed and predicted transit time for TOI-899b is presented in Figure 3 as a function of the transit number. No significant variations in transit timing are identified.

### 5. Discussion

Figure 13 shows how the physical properties of the two new transiting planets presented in this study compare to those of the current population of planetary and sub-stellar objects. According to the classification presented in Chen & Kipping (2017) TOI-883b and TOI-899b fall in the so-called Neptunian region, where the steepest variation in radius as a function of mass is observed for planetary objects. This abrupt change in their physical properties is possibly produced by the different envelope accretion histories that these objects can present before reaching a limiting mass

Table 1: Stellar parameters of TOI-883 and TOI-899.

Parameter	TOI-883	TOI-899	Source
Identifying Information			
TIC ID	123846039	177162886	TIC <sup>a</sup>
GAIA ID	3101010711776425088	5267242854094212224	Gaia DR2 <sup>b</sup>
2MASS ID	J06532863-0630270	J06575823-7131230	2MASS <sup>c</sup>
R.A. (J2015.5, h:m:s)	6 <sup>h</sup> 53 <sup>m</sup> 28.57 <sup>s</sup>	6 <sup>h</sup> 57 <sup>m</sup> 58.19 <sup>s</sup>	Gaia DR2 <sup>b</sup>
DEC (J2015.5, d:m:s)	-6°30'28.21"	-70°31'23.18"	Gaia DR2 <sup>b</sup>
Proper motion and parallax			
$\mu_\alpha \cos \delta$ (mas yr <sup>-1</sup> )	-50.2 ± 0.1	-6.95 ± 0.04	Gaia DR2 <sup>b</sup>
$\mu_\delta$ (mas yr <sup>-1</sup> )	-76.0 ± 0.1	0.83 ± 0.04	Gaia DR2 <sup>b</sup>
Parallax (mas)	9.71 ± 0.03	3.25 ± 0.02	Gaia DR2 <sup>b</sup>
Spectroscopic properties			
$T_{\text{eff}}$ (K)	5697 ± 80	5696 ± 80	ZASPE <sup>d</sup>
Spectral Type	G	G	ZASPE <sup>d</sup>
[Fe/H] (dex)	0.02 ± 0.04	0.10 ± 0.04	ZASPE <sup>d</sup>
$\log g_*$ (cgs)	4.429 ± 0.022	4.355 ± 0.022	ZASPE <sup>d</sup>
$v \sin(i_*)$ (km/s)	2.53 ± 0.30	3.65 ± 0.30	ZASPE <sup>d</sup>
Photometric properties			
$T$ (mag)	9.372 ± 0.006	11.587 ± 0.006	TIC <sup>a</sup>
$G$ (mag)	9.8279 ± 0.0004	12.0666 ± 0.0002	Gaia DR2 <sup>b</sup>
$B$ (mag)	10.574 ± 0.071	12.968 ± 0.027	Tycho-2 <sup>e</sup>
$V$ (mag)	9.957 ± 0.005	12.25 ± 0.010	Tycho-2 <sup>e</sup>
$J$ (mag)	8.749 ± 0.026	10.928 ± 0.024	2MASS <sup>c</sup>
$H$ (mag)	8.437 ± 0.038	10.599 ± 0.024	2MASS <sup>c</sup>
$Ks$ (mag)	8.37 ± 0.023	10.51 ± 0.021	2MASS <sup>c</sup>
Derived properties			
$M_*$ ( $M_\odot$ )	0.956 <sup>+0.054</sup> <sub>-0.051</sub>	0.972 <sup>+0.054</sup> <sub>-0.053</sub>	PARSEC*
$R_*$ ( $R_\odot$ )	0.988 <sup>+0.012</sup> <sub>-0.012</sub>	1.086 <sup>+0.013</sup> <sub>-0.012</sub>	PARSEC*
$L_*$ ( $L_\odot$ )	0.934 <sup>+0.043</sup> <sub>-0.031</sub>	1.113 <sup>+0.054</sup> <sub>-0.052</sub>	PARSEC*
$A_v$ (mag)	0.08 <sup>+0.06</sup>	0.18 <sup>+0.069</sup> <sub>-0.072</sub>	PARSEC*
Age (Gyr)	6.5 <sup>+2.0</sup> <sub>-2.1</sub>	8.4 <sup>+2.0</sup> <sub>-2.0</sub>	PARSEC*
$\rho_*$ (g cm <sup>-3</sup> )	1.40 <sup>+0.15</sup> <sub>-0.14</sub>	1.07 <sup>+0.11</sup> <sub>-0.10</sub>	PARSEC*

Note. Logarithms given in base 10.

(a) TESS Input Catalog (Stassun et al. 2019); (b) Gaia Data Release 2 (Gaia Collaboration et al. 2018); (c) Two-micron All Sky Survey (Cutri et al. 2003); (d) Zonal Atmospheric Stellar Parameters Estimator (Brahm et al. 2015, 2017b); (e) Tycho-2 Catalog (Høg et al. 2000)

\*: PARSEC isochrones (Bressan et al. 2012); using stellar parameters obtained from ZASPE.

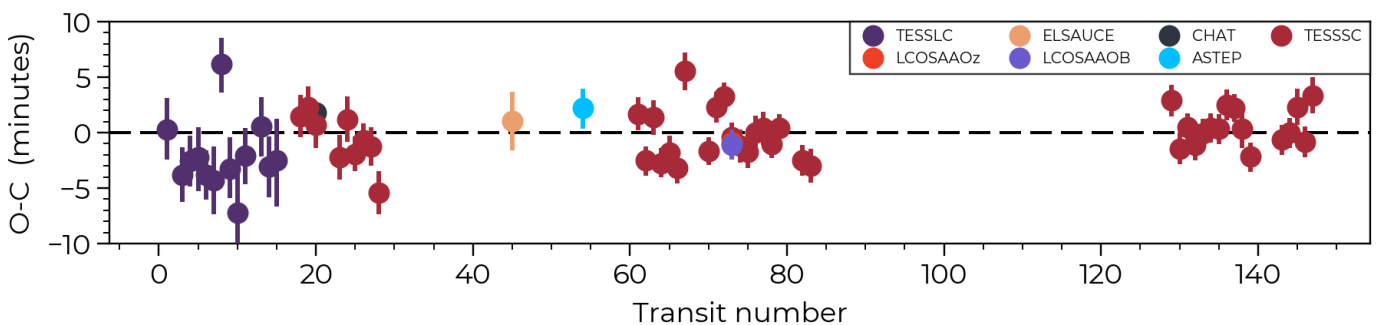


Fig. 3: Observed minus calculated diagram of all the transits observed for TOI-899b. No significant periodic signal was found in the data, ruling out an additional companion found via TTVs.

around that of Saturn, where a gaseous dominated structure becomes partially electron degenerate.

TOI-883b and TOI-899b orbit main sequence solar-type stars with solar-like metallicities and have similar orbital periods (10.1 days and 12.8 days, respectively). Despite this, the two

planets seem to have remarkably different physical structures, which is further highlighted in Figure 14. While the radius of TOI-883b is relatively similar to that of Neptune (1.76 Neptune radii), TOI-899b has an inflated radius of 2.88 Neptune radii. Their masses also show some discrepancy, with TOI-883b hav-

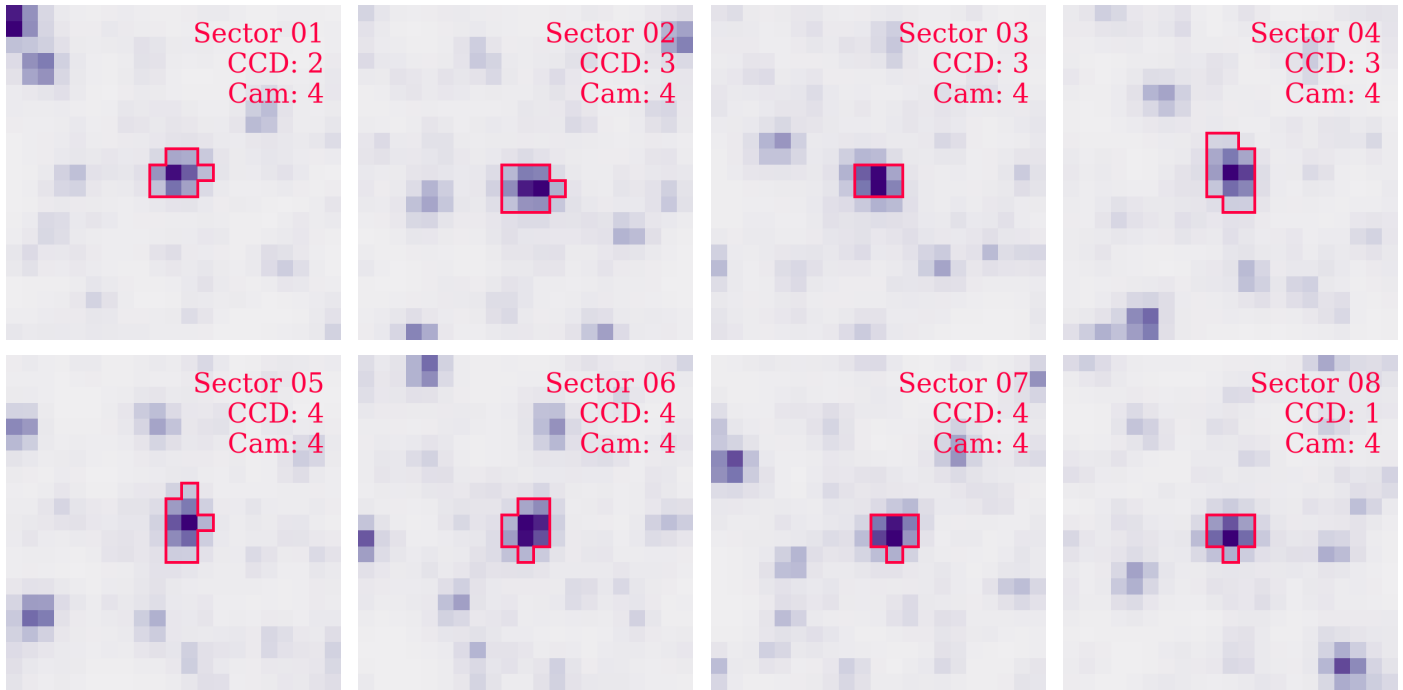


Fig. 4: TOI-899 as seen on TESS Sectors 1 to 8, which are only available in Long Cadence. As the field of view rotates, the star falls on different CCD, showing different shapes and neighborhoods, which can affect the noise of the light curve. The aperture chosen for each sector is highlighted in red.

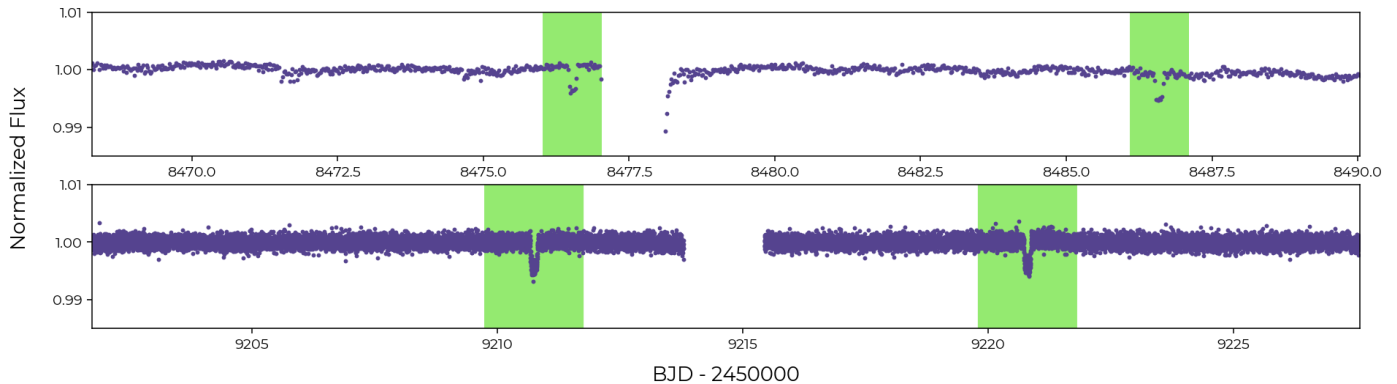


Fig. 5: TESS Light curve for TOI-883. Top panel corresponds to long cadence data from Sector 6 and bottom panel short cadence from Sector 33.

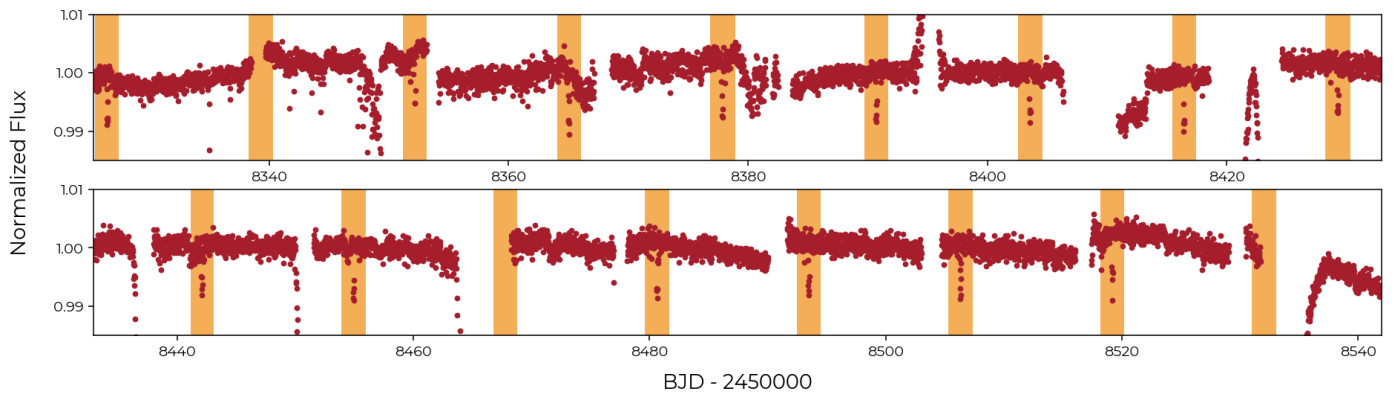


Fig. 6: Long cadence TESS light curve for TOI-899. Data is taken from Sectors 1 to 8, with a total span of 217 days. TOI-899b transits are highlighted in orange. Three of them are missing due to data gaps.

Table 2: Adopted priors for the joint transit and RV analysis on both targets.  $\mathcal{N}$ ,  $\mathcal{U}$ ,  $\mathcal{J}$  corresponds to normal, uniform and Jeffreys (log-uniform) distributions, respectively. Values reported are after choosing between eccentric and non-eccentric models.

Parameter name	Prior for TOI-883b	Prior for TOI-899b	Units	Description
Star				
$\rho_*$	$\mathcal{N}(1397, 87^2)$	$\mathcal{N}(1071, 100^2)$	kg/m <sup>3</sup>	Stellar density.
Planet b				
$P_b$	$\mathcal{N}(10.06, 0.02^2)$	$\mathcal{N}(12.84, 0.02^2)$	days	Period.
$t_{0,b}$	$\mathcal{N}(2458466.46, 0.02^2)$	$\mathcal{N}(2458313.63, 0.02^2)$	days	Time of transit-center.
$r_{1,b}$	$\mathcal{U}(0, 1)$	$\mathcal{U}(0, 1)$	—	Parametrization for $p$ and $b$ .
$r_{2,b}$	$\mathcal{U}(0, 1)$	$\mathcal{U}(0, 1)$	—	Parametrization for $p$ and $b$ .
$K_b$	$\mathcal{U}(0, 100)$	$\mathcal{U}(0, 100)$	m/s	Radial-velocity semi-amplitude.
$e_b$	0 (fixed)	$\mathcal{U}(0, 0.9)$	—	Eccentricity.
$\omega$	90 (fixed)	$\mathcal{U}(0, 360)$	—	Argument of periaxis.
TESS (30-min)				
$D_{\text{TESSLC}}$	$\mathcal{U}(0, 1)$	$\mathcal{U}(0, 1)$	—	Dilution factor for TESS.
$M_{\text{TESSLC}}$	$\mathcal{N}(0, 0.1^2)$	$\mathcal{N}(0, 0.1^2)$	ppm	Relative flux offset for TESS.
$\sigma_{w,\text{TESSLC}}$	$\mathcal{J}(10^{-4}, 5000)$	$\mathcal{J}(0.1, 5000)$	ppm	Extra jitter term for TESS lightcurve.
$q_{1,\text{TESSLC+TESSSC}}$	$\mathcal{U}(0, 1)$	$\mathcal{U}(0, 1)$	—	Quadratic LD parametrization.
$q_{2,\text{TESSLC+TESSSC}}$	$\mathcal{U}(0, 1)$	$\mathcal{U}(0, 1)$	—	Quadratic LD parametrization.
TESS (2-min)				
$D_{\text{TESSSC}}$	1 (fixed)	1 (fixed)	—	Dilution factor for TESS.
$M_{\text{TESSSC}}$	$\mathcal{N}(0, 0.1^2)$	$\mathcal{N}(0, 0.1^2)$	ppm	Relative flux offset for TESS.
$\sigma_{w,\text{TESSSC}}$	0 (fixed)	0 (fixed)	ppm	Extra jitter term for TESS lightcurve.
CHAT				
$D_{\text{CHAT}}$	1 (fixed)	1 (fixed)	—	Dilution factor for CHAT.
$M_{\text{CHAT}}$	$\mathcal{N}(0, 0.1^2)$	$\mathcal{N}(0, 0.1^2)$	ppm	Relative flux offset for CHAT.
$\sigma_{w,\text{CHAT}}$	$\mathcal{J}(10^{-4}, 5000)$	$\mathcal{J}(10^{-2}, 1000)$	ppm	Extra jitter term for CHAT lightcurve.
$q_{1,\text{CHAT}}$	$\mathcal{U}(0, 1)$	$\mathcal{U}(0, 1)$	—	Linear LD parametrization.
El Sauce				
$D_{\text{ELSAUCE}}$	—	1 (fixed)	—	Dilution factor for El Sauce.
$M_{\text{ELSAUCE}}$	—	$\mathcal{N}(0, 0.1^2)$	ppm	Relative flux offset for El Sauce.
$\sigma_{w,\text{ELSAUCE}}$	—	$\mathcal{J}(10^{-2}, 1000)$	ppm	Extra jitter term for El Sauce lightcurve.
$q_{1,\text{ELSAUCE}}$	—	$\mathcal{U}(0, 1)$	—	Linear LD parametrization.
LCO (CTIO)				
$D_{\text{LCOCTIO}}$	1 (fixed)	—	—	Dilution factor for LCO/CTIO.
$M_{\text{LCOCTIO}}$	$\mathcal{N}(0, 0.1^2)$	—	ppm	Relative flux offset for LCO/CTIO.
$\sigma_{w,\text{LCOCTIO}}$	$\mathcal{J}(10^{-2}, 5000)$	—	ppm	Extra jitter term for LCO/CTIO.
$q_{1,\text{LCOCTIO}}$	$\mathcal{U}(0, 1)$	—	—	Linear LD parametrization.
LCO (MCD)				
$D_{\text{LCOMCD}}$	1 (fixed)	—	—	Dilution factor for LCO/MCD.
$M_{\text{LCOMCD}}$	$\mathcal{N}(0, 0.1^2)$	—	ppm	Relative flux offset for LCO/MCD.
$\sigma_{w,\text{LCOMCD}}$	$\mathcal{J}(10^{-2}, 5000)$	—	ppm	Extra jitter term for LCO/MCD.
$q_{1,\text{LCOMCD}}$	$\mathcal{U}(0, 1)$	—	—	Linear LD parametrization.
RV parameters				
$\mu_{\text{FEROS}}$	$\mathcal{N}(16617.1, 20^2)$	$\mathcal{N}(44695, 20^2)$	m/s	Systemic velocity for FEROS.
$\sigma_{w,\text{FEROS}}$	$\mathcal{J}(10^{-6}, 0.2)$	$\mathcal{J}(10^{-4}, 200)$	m/s	Extra jitter term for FEROS.
$\mu_{\text{HARPS}}$	$\mathcal{N}(16647.5, 20^2)$	$\mathcal{N}(44710, 20^2)$	m/s	Systemic velocity for HARPS.
$\sigma_{w,\text{HARPS}}$	$\mathcal{J}(10^{-6}, 0.2)$	$\mathcal{J}(10^{-4}, 200)$	m/s	Extra jitter term for HARPS.
$\mu_{\text{PFS}}$	$\mathcal{N}(0.002, 0.2^2)$	—	m/s	Systemic velocity for PFS.
$\sigma_{w,\text{PFS}}$	$\mathcal{J}(10^{-6}, 0.2)$	—	m/s	Extra jitter term for PFS.
$\mu_{\text{CHIRON}}$	—	$\mathcal{U}(43000, 44000)$	m/s	Systemic velocity for CHIRON.
$\sigma_{w,\text{CHIRON}}$	—	$\mathcal{J}(10^{-4}, 200)$	m/s	Extra jitter term for CHIRON.

ing a mass of 0.12 Jupiter masses and TOI-899b 0.2 Jupiter masses. Due to their moderately long periods and mild insolation levels, the internal structure of both planets is not expected to be significantly affected by stellar radiative, tidal, and/or magnetic effects (Spiegel & Burrows 2013), and in turn, these differences in structure can inform us about the varied composition that a gi-

ant planet can have depending on the disk conditions where they were formed.

The radius of TOI-883b aligns with traditional structural models by suggesting a moderate enrichment of heavy elements. Utilizing the models from Fortney et al. (2007), which assume that all heavy elements are situated in the planet's core, we de-

Table 3: Evidences for preliminary RV analysis in TOI-883 and TOI-899 systems. No signs of non-transiting planets were found.

Model	TOI-883b		TOI-899b	
	ln Z	Δ ln Z	ln Z	Δ ln Z
1 planet circular	147.85	0	101.41	0
1 planet eccentric	147.67	-0.18	99.72	-1.69
inner circular + outer circular	147.19	-0.66	98.17	-3.24
inner circular + outer eccentric	147.17	-0.68	98.45	-2.96
inner eccentric + outer circular	146.76	-1.09	96.51	-4.9
inner eccentric + outer eccentric	145.95	-1.9	96.16	-5.25
no planets	121.09	-26.76	91.05	-10.36

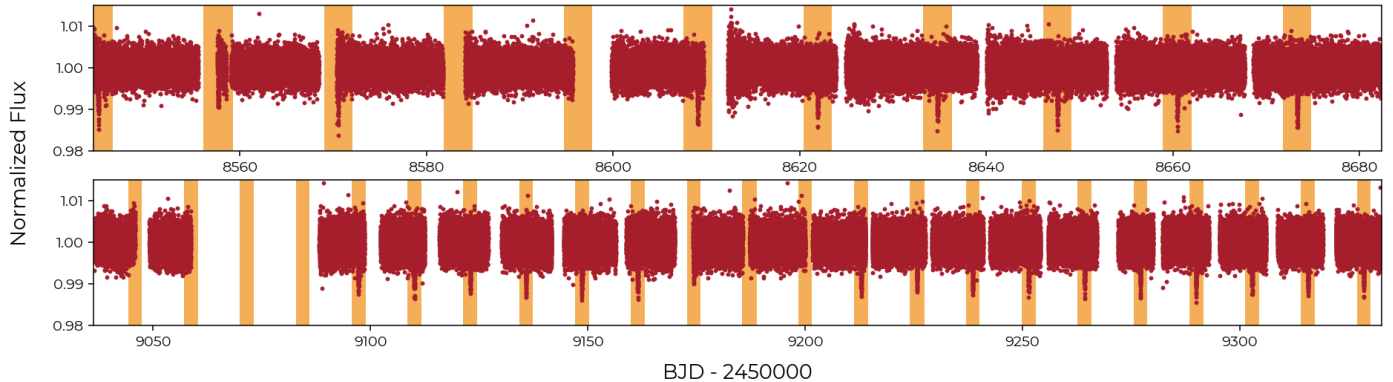


Fig. 7: Short cadence TESS light curve for TOI-899. Top panel shows data from Sectors 9 to 13. Bottom data comes from Sectors 27 and 29 to 37. Transit occurrences are highlighted in orange.

Table 4: Calculated evidence returned by Juliet for the case comparing eccentric vs non-eccentric model. For TOI-883b a non-eccentric model is favored, meanwhile, for TOI-899b an eccentric one is chosen.

Model	TOI-883b	TOI-899b
Eccentric	112143.030	300242.699
Non-eccentric	112158.073	300231.038

determine that a core mass of  $M_c = 25.03 \pm 2.55 M_{\oplus}$  is adequate to account for the planet's mass and radius. A slightly lower level of heavy element enrichment could be achieved with more recent models (e.g. Thorngren et al. 2016), which allows some solids to be distributed within the gaseous envelope. TOI-883b, according to some recent formation models, could have formed at long distances from the central star, where high envelope luminosity due to the constant inflow of pebbles prevents the core from reaching the threshold mass required to trigger the runaway gaseous accretion before the disk dispersal (Bitsch et al. 2015; Chen et al. 2020; Brouwers et al. 2021). The challenge in adopting this formation scenario for TOI-883b is to explain its current short semi-major axis. A disk-driven migration for this planet would suggest accessing the inner areas of the disk where the pebble isolation mass is reachable, leading to the rapid development of a gas giant. Scenarios involving high eccentricity migration (e.g. Rasio & Ford 1996; Wu & Murray 2003; Naoz et al. 2012), particularly after the disk has dissipated, are plausible explanations for the current characteristics of TOI-883b. This could also account for its mild eccentricity and the absence of other large, nearby planets in the system. Among the currently known population of well-characterized transiting planets, TOI-883b closely resembles HATS-7b (Bakos et al. 2015), which has a radius of 0.57

$R_{\text{J}}$  and a mass of  $0.12 M_{\text{J}}$ . In comparison, TOI-883b has a radius of  $0.605 R_{\text{J}}$  and a mass of  $0.124 M_{\text{J}}$ . However, HATS-7b orbits a cooler K-type star and has a shorter orbital period of 3.2 days. Additionally, K2-234b (Yu et al. 2018) shares similar physical characteristics with TOI-883b and has a moderately longer orbital period of 11.8 days, but it orbits a slightly more massive subgiant star.

TOI-899b, on the other hand, is a significantly less dense sub-Saturn. By using the Fortney et al. (2007) models for the properties of the TOI-899 system, we find that this planet is consistent with having a core-less interior ( $M_c = 0.29 \pm 1.53 M_{\oplus}$ ), being completely dominated by a gaseous structure. Specifically, we can put an upper limit of  $4 M_{\oplus}$  for the bulk heavy element enrichment of TOI-899b. The other three sub-Saturns with low irradiation and masses compatible with TOI-899b (Kepler-34b, Welsh et al. 2012; TOI-1456b, Dalba et al. 2020; TOI-197b, Huber et al. 2019), all have radii below  $0.9 R_{\text{J}}$  which implies the presence of a massive central core of  $10-20 M_{\oplus}$ , more in line with the expectations of the core accretion theory.

Both planets presented here pose an additional challenge to planet formation models: their masses fall into a valley of low occurrence predicted by core accretion models (e.g., Ida & Lin 2004; Mordasini et al. 2009; Emsenhuber et al. 2021; Burn et al. 2021; Schlecker et al. 2021, 2022) due to the rapid growth via runaway gas accretion of planets reaching a mass above  $\sim 10 M_{\oplus}$  (Mizuno et al. 1978; Pollack et al. 1996). This predicted bimodality in the mass distribution of giant exoplanets has been tentatively detected in homogeneously derived samples of radial velocity-detected planets (Mayor et al. 2011) but appears absent in more recently collected planet populations discovered with the RV (Sabotta et al. 2021; Schlecker et al. 2022; Ribas et al. 2023) and microlensing techniques (Suzuki et al. 2016, 2018; Bennett et al. 2021). The absence of this “sub-Saturn valley” has

Table 5: TOI-883b and TOI-899b parameters.

Parameter name	Posterior for TOI-883b	Posterior for TOI-899b	Units	Description
Parameters for the star				
$\rho_*$	$1408^{+74}_{-78}$	$1110^{+80}_{-86}$	kg/m <sup>3</sup>	Stellar density.
Parameters for planet b				
$P_b$	$10.05772^{+0.00002}_{-0.00002}$	$12.84618^{+0.00001}_{-0.00001}$	days	Period.
$t_{0,b}$	$2458466.4730^{+0.0012}_{-0.0013}$	$2458313.63758^{+0.00043}_{-0.00044}$	days	Time of transit-center.
$r_{1,b}$	$0.657^{+0.023}_{-0.024}$	$0.828^{+0.021}_{-0.023}$	—	Parametrization for $p$ and $b$ .
$r_{2,b}$	$0.063^{+0.001}_{-0.001}$	$0.094^{+0.001}_{-0.002}$	—	Parametrization for $p$ and $b$ .
$K_b$	$11.926^{+0.961}_{-0.945}$	$18.685^{+2.020}_{-1.990}$	m/s	Radial-velocity semi-amplitude.
$e_b$	0 (fixed)	$0.218^{+0.054}_{-0.057}$	—	Eccentricity.
$\omega$	90 (fixed)	$128.526^{+14.743}_{-17.869}$	—	Argument of periaxis.
Parameters for TESS (30-min)				
$D_{\text{TESSLC}}$	$0.972^{+0.018}_{-0.028}$	$0.981^{+0.012}_{-0.016}$	—	Dilution factor for TESS.
$\sigma_{w,\text{TESSLC}}$	$202^{+20}_{-20}$	$739.800^{+25.445}_{-25.977}$	ppm	Extra jitter term for TESS lightcurve.
$q_{1,\text{TESSLC+TESSSC}}$	$0.550^{+0.211}_{-0.185}$	$0.253^{+0.075}_{-0.059}$	—	Quadratic LD parametrization.
$q_{2,\text{TESSLC+TESSSC}}$	$0.123^{+0.148}_{-0.079}$	$0.773^{+0.147}_{-0.209}$	—	Quadratic LD parametrization.
Parameters for TESS (2-min)				
$D_{\text{TESSSC}}$	1 (fixed)	1 (fixed)	—	Dilution factor for TESS.
$\sigma_{w,\text{TESSSC}}$	0 (fixed)	0 (fixed)	ppm	Extra jitter term for TESS lightcurve.
Parameters for CHAT				
$D_{\text{CHAT}}$	1 (fixed)	1 (fixed)	—	Dilution factor for CHAT.
$\sigma_{w,\text{CHAT}}$	$3607^{+132}_{-121}$	$997.838^{+1.491}_{-2.774}$	ppm	Extra jitter term for CHAT lightcurve.
$q_{1,\text{CHAT}}$	$0.495^{+0.237}_{-0.260}$	$0.545^{+0.107}_{-0.119}$	—	Linear LD parametrization.
Parameters for El Sauce				
$D_{\text{ELSAUCE}}$	—	1 (fixed)	—	Dilution factor for El Sauce.
$\sigma_{w,\text{ELSAUCE}}$	—	$2.042^{+90.193}_{-1.976}$	ppm	Extra jitter term for El Sauce lightcurve.
$q_{1,\text{ELSAUCE}}$	—	$0.785^{+0.138}_{-0.219}$	—	Linear LD parametrization.
Parameters for LCO (CTIO)				
$D_{\text{LCOCTIO}}$	1 (fixed)	—	—	Dilution factor for LCO/CTIO.
$\sigma_{w,\text{LCOCTIO}}$	$0.2^{+20}_{-0.2}$	—	ppm	Extra jitter term for LCO/CTIO.
$q_{1,\text{LCOCTIO}}$	$0.39^{+0.16}_{-0.17}$	—	—	Linear LD parametrization.
Parameters for LCO (MCD)				
$D_{\text{LCOMCD}}$	1 (fixed)	—	—	Dilution factor for LCO/MCD.
$\sigma_{w,\text{LCOMCD}}$	$0.17^{+23.66}_{-0.16}$	—	ppm	Extra jitter term for LCO/MCD.
$q_{1,\text{LCOMCD}}$	$0.710^{+0.179}_{-0.225}$	—	—	Linear LD parametrization.
RV parameters				
$\mu_{\text{FEROS}}$	$16615.36^{+2.68}_{-2.57}$	$44697.329^{+3.834}_{-3.926}$	m/s	Systemic velocity for FEROS.
$\sigma_{w,\text{FEROS}}$	$10.51^{+2.50}_{-2.07}$	$23.098^{+3.128}_{-2.750}$	m/s	Extra jitter term for FEROS.
$\mu_{\text{HARPS}}$	$16648.28^{+1.39}_{-1.34}$	$44713.701^{+1.848}_{-1.709}$	m/s	Systemic velocity for HARPS.
$\sigma_{w,\text{HARPS}}$	$4.65^{+1.34}_{-0.99}$	$0.021^{+0.572}_{-0.020}$	m/s	Extra jitter term for HARPS.
$\mu_{\text{PFS}}$	$0.82^{+0.86}_{-0.88}$	—	m/s	Systemic velocity for PFS.
$\sigma_{w,\text{PFS}}$	$2.64^{+0.88}_{-0.62}$	—	m/s	Extra jitter term for PFS.
$\mu_{\text{CHIRON}}$	—	$43302.230^{+10.865}_{-11.197}$	m/s	Systemic velocity for CHIRON.
$\sigma_{w,\text{CHIRON}}$	—	$0.068^{+2.092}_{-0.067}$	m/s	Extra jitter term for CHIRON.

been hypothesized to point to oversimplifications in classical 1D hydrostatic gas accretion models (Szulágyi et al. 2014; Moldenhauer et al. 2021; Schlecker et al. 2022; Krapp et al. 2022). Planets on intermediate orbits and with masses like TOI-883b and TOI-899b are a valuable contribution to a sparse sample that will help to characterize the existence and shape of the mass valley, which may constrain planetary gas accretion theories.

Future detailed follow-up observations of TOI-883b and TOI-899b could contribute to unveiling their formation histo-

ries in this and other regards. Having transmission spectroscopy metrics (Kempton et al. 2018a) of 235 and 180, respectively, both systems are suitable targets for atmospheric characterization (see Figure 15). In this context, the determination of their atmospheric metallicities (e.g. Wong et al. 2020) could further help to constrain the properties of the regions of the protoplanetary disk where they were formed. Additionally, due to their moderately long periods and mild tidal interactions, both systems are interesting targets for measuring their projected stel-

Table 6: Derived planetary parameters obtained for TOI-883b and TOI-899b using the posterior values from Table 5.  $T_{eq}$  was calculated using equation 16 from [Méndez & Rivera-Valentín \(2017\)](#), assuming an albedo  $A = 0$  and a heat redistribution  $\beta = 0.5$

Parameter name	Posterior estimate	
	TOI-883b	TOI-899b
Posterior parameters		
$P_b$ (days)	$10.057716^{+0.000016}_{-0.000016}$	$12.846185^{+0.000008}_{-0.000008}$
$t_{0,b}$ (BJD UTC)	$2458466.473005^{+0.001214}_{-0.001252}$	$2458313.637577^{+0.000434}_{-0.000441}$
$\rho_*$ ( $\text{kg/m}^3$ )	$1408^{+74}_{-78}$	$1110^{+80}_{-86}$
$r_{1,b}$	$0.6572^{+0.0232}_{-0.0240}$	$0.8277^{+0.0206}_{-0.0229}$
$r_{2,b}$	$0.0628^{+0.0008}_{-0.0008}$	$0.0937^{+0.0012}_{-0.0015}$
$K_b$ (m/s)	$11.926^{+0.961}_{-0.945}$	$18.685^{+2.020}_{-1.990}$
$e_b$	0 (fixed)	$0.218^{+0.054}_{-0.057}$
Transit parameters		
$R_p/R_\star$	$0.0628^{+0.0008}_{-0.0008}$	$0.0937^{+0.0012}_{-0.0015}$
$b = (a/R_\star) \cos(i_p)$	$0.49^{+0.03}_{-0.04}$	$0.742^{+0.030}_{-0.034}$
$a_b/R_\star$	$19.55^{+0.99}_{-0.99}$	$21.316^{+0.502}_{-0.564}$
$i_p$ (deg)	$88.58^{+0.12}_{-0.13}$	$87.572^{+0.125}_{-0.150}$
$q_{1,TESS}$	$0.55^{+0.21}_{-0.18}$	$0.25^{+0.07}_{-0.06}$
$q_{2,TESS}$	$0.12^{+0.15}_{-0.08}$	$0.77^{+0.15}_{-0.21}$
Physical parameters		
$M_p (M_J)$	$0.123 \pm 0.012$	$0.213 \pm 0.024$
$R_p (R_J)$	$0.604 \pm 0.028$	$0.991 \pm 0.044$
$a$ (AU)	$0.0898 \pm 0.0023$	$0.1063 \pm 0.0026$
$T_{eq}$ (K)	$1086 \pm 19$	$1040 \pm 19$

lar obliquities through the Rossiter-McLaughlin (RM) effect for constraining migration scenarios. TOI-883b and TOI-899b have expected RM semi-amplitude of  $5.8 \text{ ms}^{-1}$  m/s and  $14 \text{ ms}^{-1}$ , respectively for aligned orbits.

**Acknowledgements.** FR, RB, AJ and MH acknowledge support from project IC120009 “Millennium Institute of Astrophysics (MAS)” of the Millennium Science Initiative, Chilean Ministry of Economy. RB acknowledges support from FONDECYT project 1241963. AJ acknowledges additional support from FONDECYT project 1171208. MTP acknowledges support by FONDECYT-ANID Post-doctoral fellowship no. 3210253. TT acknowledges support by the BNSF program “VIHREN-2021” project No. KP-06-DV/5. The results reported herein benefited from collaborations and/or information exchange within NASA’s Nexus for Exoplanet System Science (NExSS) research coordination network sponsored by NASA’s Science Mission Directorate under Agreement No. 80NSSC21K0593 for the program “Alien Earths”. This work makes use of observations from the LCOGT network. Part of the LCOGT telescope time was granted by NOIRLab through the Mid-Scale Innovations Program (MSIP). MSIP is funded by NSF. KAC acknowledges support from the TESS mission via subaward s3449 from MIT. The postdoctoral fellowship of KB is funded by F.R.S.-FNRS grant T.0109.20 and by the Francqui Foundation. This research has made use of the Exoplanet Follow-up Observation Program (ExoFOP; DOI: 10.26134/ExoFOP5) website, which is operated by the California Institute of Technology, under contract with the National Aeronautics and Space Administration under the Exoplanet Exploration Program. This paper includes data collected with the TESS mission, obtained from the Mikulski Archive for Space Telescopes (MAST) data archive at the Space Telescope Science Institute (STScI). Funding for the TESS mission is provided by the NASA Explorer Program. STScI is operated by the Association of Universities for Research in Astronomy, Inc., under NASA contract NAS 5-26555. We acknowledge the use of public TESS data from pipelines at the TESS Science Office and at the TESS Science Processing Operations Center. Resources supporting this work were provided by the NASA High-End Computing (HEC) Program through the NASA Advanced Supercomputing (NAS) Division at Ames Research Center for the production of the SPOC data products. Based on observations made with ESO Telescopes at the La Silla Paranal Observatory under program ID 0103.C – 0442

(PI RB). This work makes use of observations from the Las Cumbres Observatory global telescope network.

## References

- Abe, L., Gonçalves, I., Agabi, A., et al. 2013, A&A, 553, A49
- Addison, B. C., Wright, D. J., Nicholson, B. A., et al. 2021, MNRAS, 502, 3704
- Bakos, G. Á., Penev, K., Bayliss, D., et al. 2015, ApJ, 813, 111
- Bakos, G. Á., Torres, G., Pál, A., et al. 2010, ApJ, 710, 1724
- Barragán, O., Grziwa, S., Gandolfi, D., et al. 2016, AJ, 152, 193
- Bayliss, D., Hartman, J. D., Bakos, G. Á., et al. 2015, AJ, 150, 49
- Bennett, D. P., Ranc, C., & Fernandes, R. B. 2021, The Astronomical Journal, 162, 243
- Bitsch, B., Lambrechts, M., & Johansen, A. 2015, A&A, 582, A112
- Borucki, W. J., Koch, D., Basri, G., et al. 2010, Science, 327, 977
- Bozhilov, V., Antonova, D., Hobson, M. J., et al. 2023, ApJ, 946, L36
- Bradley, L., Sipőcz, B., Robitaille, T., et al. 2019, astropy/photutils: v0.7.2
- Brady, M. T., Petigura, E. A., Knutson, H. A., et al. 2018, AJ, 156, 147
- Brahm, R., Espinoza, N., Jordán, A., et al. 2019a, AJ, 158, 45
- Brahm, R., Espinoza, N., Jordán, A., et al. 2019b, AJ, 158, 45
- Brahm, R., Espinoza, N., Rabus, M., et al. 2019c, MNRAS, 483, 1970
- Brahm, R., Jordán, A., & Espinoza, N. 2017a, PASP, 129, 034002
- Brahm, R., Jordán, A., Hartman, J., & Bakos, G. 2017b, MNRAS, 467, 971
- Brahm, R., Jordán, A., Hartman, J. D., et al. 2015, AJ, 150, 33
- Brahm, R., Nielsen, L. D., Wittenmyer, R. A., et al. 2020, AJ, 160, 235
- Brahm, R., Ulmer-Möll, S., Hobson, M. J., et al. 2023, AJ, 165, 227
- Brasseur, C. E., Phillip, C., Fleming, S. W., Mullally, S. E., & White, R. L. 2019, Astrocut: Tools for creating cutouts of TESS images
- Bressan, A., Marigo, P., Girardi, L., et al. 2012, MNRAS, 427, 127
- Brouwers, M. G., Ormel, C. W., Bonsor, A., & Vazan, A. 2021, A&A, 653, A103
- Brown, T. M., Baliber, N., Bianco, F. B., et al. 2013, PASP, 125, 1031
- Buchhave, L. A., Latham, D. W., Johansen, A., et al. 2012, Nature, 486, 375
- Buchner, J., Georgakakis, A., Nandra, K., et al. 2014, A&A, 564, A125
- Burke, C. J., Levine, A., Fausnaugh, M., et al. 2020, TESS-Point: High precision TESS pointing tool

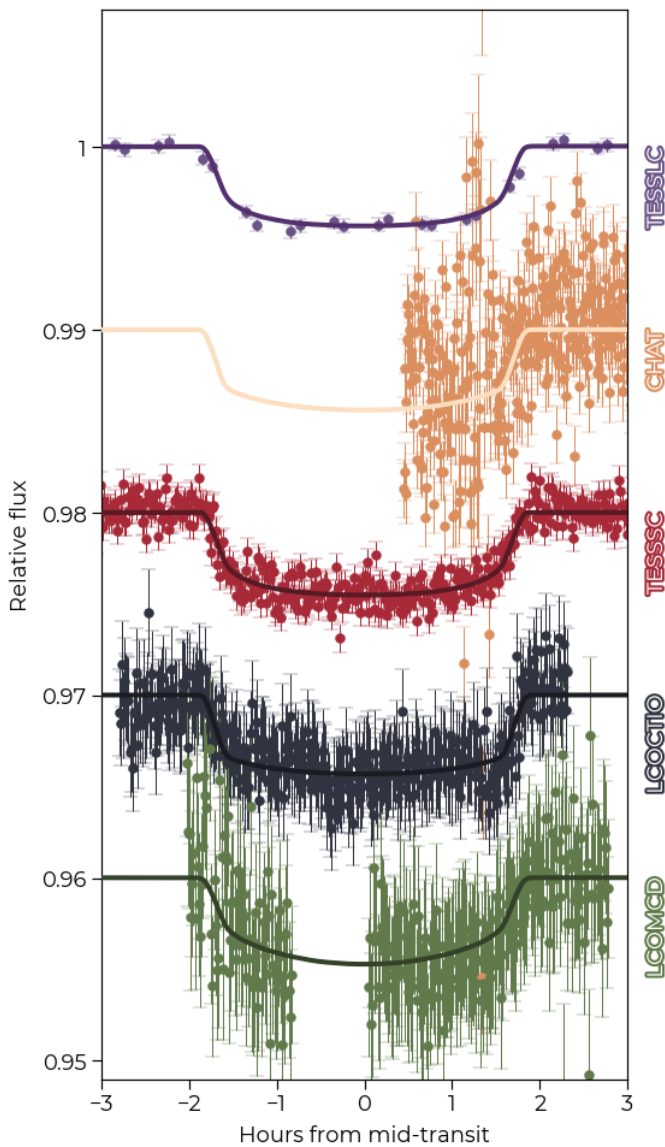


Fig. 8: Photometric observations and transits for TOI-883b. In the case of TESS, both light curves are phase folded. CHAT and both from Las Cumbres Observatory are follow-up data that observed a single transit.

Burn, R., Schlecker, M., Mordasini, C., et al. 2021, *Astronomy & Astrophysics*, 656, A72  
 Butler, R. P., Marcy, G. W., Williams, E., et al. 1996, *PASP*, 108, 500  
 Cardelli, J. A., Clayton, G. C., & Mathis, J. S. 1989, *ApJ*, 345, 245  
 Castelli, F. & Kurucz, R. L. 2004, New Grids of ATLAS9 Model Atmospheres  
 Castelli, F. & Kurucz, R. L. 2006, *A&A*, 454, 333  
 Chen, J. & Kipping, D. 2017, *ApJ*, 834, 17  
 Chen, Y.-X., Li, Y.-P., Li, H., & Lin, D. N. C. 2020, *ApJ*, 896, 135  
 Collins, K. A., Kielkopf, J. F., Stassun, K. G., & Hessman, F. V. 2017, *AJ*, 153, 77

Colón, K. D., Kreidberg, L., Line, M., et al. 2020, *arXiv e-prints*, arXiv:2005.05153  
 Crane, J. D., Shectman, S. A., & Butler, R. P. 2006, in *Society of Photo-Optical Instrumentation Engineers (SPIE) Conference Series*, Vol. 6269, *Ground-based and Airborne Instrumentation for Astronomy*, ed. I. S. McLean & M. Iye, 626931  
 Crane, J. D., Shectman, S. A., Butler, R. P., et al. 2010, *Society of Photo-Optical Instrumentation Engineers (SPIE) Conference Series*, Vol. 7735, *The Carnegie Planet Finder Spectrograph: integration and commissioning*, 773553  
 Crane, J. D., Shectman, S. A., Butler, R. P., Thompson, I. B., & Burley, G. S. 2008, *Society of Photo-Optical Instrumentation Engineers (SPIE) Conference*

Table 7: Radial velocity data obtained for TOI-883b.

BJD - 2450000	Radial Velocity (m/s)	Bisector (m/s)
FEROS		
8553.67181	16618.3 ± 77	-34 ± 11
8627.45229	16613.4 ± 60	-23 ± 9
8626.45925	16659.4 ± 79	1 ± 11
8625.45179	16620.7 ± 72	-26 ± 11
8624.45751	16636.9 ± 88	-25 ± 12
8623.44687	16623.5 ± 81	-26 ± 12
8620.45369	16614.7 ± 65	-7 ± 10
8619.46761	16612.8 ± 64	-8 ± 10
8617.46982	16621.3 ± 57	-18 ± 9
8599.49535	16612.9 ± 55	-15 ± 9
8594.48428	16620.0 ± 59	-21 ± 9
8595.51427	16643.6 ± 78	-4 ± 11
8554.64061	16607.3 ± 63	-26 ± 10
8555.64052	16619.1 ± 56	-13 ± 9
8574.59030	16639.2 ± 82	-25 ± 12
8556.66845	16606.4 ± 67	-8 ± 10
8559.66248	16587.7 ± 64	-3 ± 10
8572.59926	16608.6 ± 64	-12 ± 10
8570.59902	16604.7 ± 64	-15 ± 10
8566.59518	16607.8 ± 55	-23 ± 9
8569.61309	16595.1 ± 56	-27 ± 9
8568.58302	16603.2 ± 56	-25 ± 9
HARPS		
8578.56809	16640.7 ± 3.0	-23 ± 4
8834.81040	16655.1 ± 2.0	-18 ± 2
8832.79213	16632.6 ± 2.3	-17 ± 3
8823.83066	16646.5 ± 2.0	-18 ± 2
8806.82846	16664.0 ± 2.0	-13 ± 2
8802.78054	16647.0 ± 2.0	-16 ± 2
8840.72423	16643.0 ± 2.0	-14 ± 2
8579.56214	16641.8 ± 2.0	-21 ± 2
8580.55407	16641.4 ± 2.0	-18 ± 2
8836.78320	16661.0 ± 2.0	-14 ± 2
8581.53267	16637.4 ± 2.0	-17 ± 2
8582.58717	16647.7 ± 2.0	-13 ± 2
8583.55616	16656.9 ± 2.0	-14 ± 2
8576.59963	16651.3 ± 3.4	-13 ± 4
PFS		
8620.46359	-10.07 ± 0.80	—
8766.87428	9.76 ± 0.71	—
8761.88540	-10.21 ± 0.78	—
8593.49024	8.57 ± 1.07	—
8595.48683	15.47 ± 1.18	—
8625.47898	15.25 ± 1.24	—
8619.47176	-7.34 ± 0.88	—
8623.47001	6.66 ± 0.74	—
8591.54149	-6.09 ± 0.99	—
8622.47493	-1.71 ± 0.77	—

Series, Vol. 7014, *The Carnegie Planet Finder Spectrograph: a status report*, 701479  
 Cutri, R. M., Skrutskie, M. F., van Dyk, S., et al. 2003, *2MASS All Sky Catalog of point sources*.  
 Dalba, P. A., Gupta, A. F., Rodriguez, J. E., et al. 2020, *AJ*, 159, 241  
 Díaz, M. R., Jenkins, J. S., Feng, F., et al. 2020, *arXiv e-prints*, arXiv:2003.10319  
 Dorval, P., Talens, G. J. J., Otten, G. P. P. L., et al. 2019, *arXiv e-prints*, arXiv:1904.02733  
 Eberhardt, J., Hobson, M. J., Henning, T., et al. 2023, *AJ*, 166, 271  
 Emsenhuber, A., Mordasini, C., Burn, R., et al. 2021, *Astronomy & Astrophysics*, 656, A70

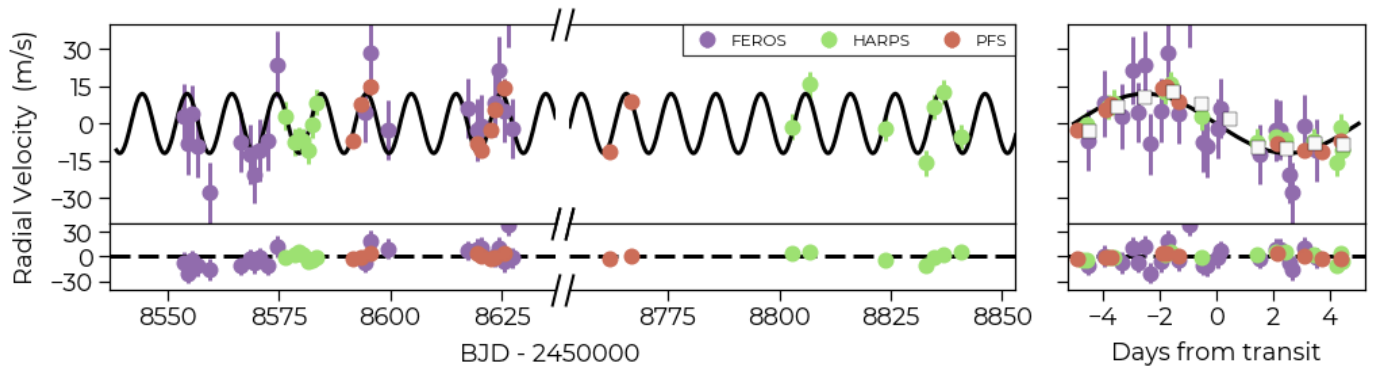


Fig. 9: Radial velocities observed for TOI-883 with FEROS (purple), HARPS (green) and PFS (orange). Phase folded radial velocity curve is plotted in the right panel. The best Keplerian model is included and plotted in black.

Espinoza, N. 2018, Research Notes of the American Astronomical Society, 2, 209

Espinoza, N., Fortney, J. J., Miguel, Y., Thorngren, D., & Murray-Clay, R. 2017, *ApJ*, 838, L9

Espinoza, N. & Jordán, A. 2016, *MNRAS*, 457, 3573

Espinoza, N., Kossakowski, D., & Brahm, R. 2018, arXiv e-prints, arXiv:1812.08549

Ester, M., Kriegel, H.-P., Sander, J., & Xu, X. 1996, in Proceedings of the Second International Conference on Knowledge Discovery and Data Mining, KDD'96 (AAAI Press), 226–231

Feroz, F., Hobson, M. P., & Bridges, M. 2009, *MNRAS*, 398, 1601

Foreman-Mackey, D., Hogg, D. W., Lang, D., & Goodman, J. 2013, *PASP*, 125, 306

Fortney, J. J., Marley, M. S., & Barnes, J. W. 2007, *ApJ*, 659, 1661

Fulton, B. J., Petigura, E. A., Blunt, S., & Sinukoff, E. 2018, *PASP*, 130, 044504

Gaia Collaboration, Brown, A. G. A., Vallenari, A., et al. 2018, *A&A*, 616, A1

Ginsburg, A., Sipőcz, B. M., Brasseur, C. E., et al. 2019, *AJ*, 157, 98

Guerrero, N. M., Seager, S., Huang, C. X., et al. 2021, *ApJS*, 254, 39

Guillot, T., Abe, L., Agabi, A., et al. 2015, *Astronomische Nachrichten*, 336, 638

Hara, N. C., Boué, G., Laskar, J., & Correia, A. C. M. 2017, *MNRAS*, 464, 1220

Hartman, J. D., Bakos, G. Á., Bayliss, D., et al. 2019, *AJ*, 157, 55

Hellier, C., Anderson, D. R., Triaud, A. H. M. J., et al. 2019, *MNRAS*, 488, 3067

Hippke, M. & Heller, R. 2019, *TLS: Transit Least Squares*

Hobson, M. J., Brahm, R., Jordán, A., et al. 2021, *AJ*, 161, 235

Hobson, M. J., Trifonov, T., Henning, T., et al. 2023, *AJ*, 166, 201

Høg, E., Fabricius, C., Makarov, V. V., et al. 2000, *A&A*, 355, L27

Holman, M. J., Fabrycky, D. C., Ragozzine, D., et al. 2010, *Science*, 330, 51

Huang, C. X., Vanderburg, A., Pál, A., et al. 2020a, *Research Notes of the American Astronomical Society*, 4, 204

Huang, C. X., Vanderburg, A., Pál, A., et al. 2020b, *Research Notes of the American Astronomical Society*, 4, 206

Huber, D., Chaplin, W. J., Chontos, A., et al. 2019, *AJ*, 157, 245

Ida, S. & Lin, D. N. C. 2004, *The Astrophysical Journal*, 604, 388

Jenkins, J. M. 2002, *ApJ*, 575, 493

Jenkins, J. M., Chandrasekaran, H., McCauliff, S. D., et al. 2010, in *Society of Photo-Optical Instrumentation Engineers (SPIE) Conference Series*, Vol. 7740, *Software and Cyberinfrastructure for Astronomy*, ed. N. M. Radziwill & A. Bridger, 77400D

Jenkins, J. M., Tenenbaum, P., Seader, S., et al. 2020, *Kepler Data Processing Handbook: Transiting Planet Search*, Kepler Science Document KSCI-19081-003, id. 9. Edited by Jon M. Jenkins.

Jenkins, J. M., Twicken, J. D., McCauliff, S., et al. 2016, in *Society of Photo-Optical Instrumentation Engineers (SPIE) Conference Series*, Vol. 9913, *Software and Cyberinfrastructure for Astronomy IV*, ed. G. Chiozzi & J. C. Guzman, 99133E

Jones, M. I., Brahm, R., Espinoza, N., et al. 2019, *A&A*, 625, A16

Jones, M. I., Reinharz, Y., Brahm, R., et al. 2024, arXiv e-prints, arXiv:2401.09657

Jordán, A., Brahm, R., Espinoza, N., et al. 2019, *AJ*, 157, 100

Jordán, A., Brahm, R., Espinoza, N., et al. 2020, *AJ*, 159, 145

Kaufer, A., Stahl, O., Tubbesing, S., et al. 1999, *The Messenger*, 95, 8

Kempton, E. M. R., Bean, J. L., Louie, D. R., et al. 2018a, *PASP*, 130, 114401

Kempton, E. M. R., Bean, J. L., Louie, D. R., et al. 2018b, *PASP*, 130, 114401

Kipping, D. M. 2010, *MNRAS*, 408, 1758

Kipping, D. M. 2013, *MNRAS*, 435, 2152

Kovács, G., Zucker, S., & Mazeh, T. 2002, *A&A*, 391, 369

Krapp, L., Kratter, K. M., & Youdin, A. N. 2022, *The Astrophysical Journal*, 928, 156

Kreidberg, L. 2015, *PASP*, 127, 1161

Kreidberg, L., Line, M. R., Thorngren, D., Morley, C. V., & Stevenson, K. B. 2018, *ApJ*, 858, L6

Lambrechts, M. & Johansen, A. 2012, *A&A*, 544, A32

Laughlin, G., Crismani, M., & Adams, F. C. 2011, *ApJ*, 729, L7

Li, J., Tenenbaum, P., Twicken, J. D., et al. 2019, *PASP*, 131, 024506

Lightkurve Collaboration, Cardoso, J. V. d. M., Hedges, C., et al. 2018, *Lightkurve: Kepler and TESS time series analysis in Python*, *Astrophysics Source Code Library*

Lund, M. N., Handberg, R., Davies, G. R., Chaplin, W. J., & Jones, C. D. 2015, *ApJ*, 806, 30

Madhusudhan, N., Bitsch, B., Johansen, A., & Eriksson, L. 2017, *MNRAS*, 469, 4102

Mayor, M., Marmier, M., Lovis, C., et al. 2011, arXiv e-prints, 1

Mayor, M., Pepe, F., Queloz, D., et al. 2003, *The Messenger*, 114, 20

McCully, C., Volgenau, N. H., Harbeck, D.-R., et al. 2018, in *Society of Photo-Optical Instrumentation Engineers (SPIE) Conference Series*, Vol. 10707, Proc. SPIE, 107070K

Mékarnia, D., Guillot, T., Rivet, J. P., et al. 2016, *MNRAS*, 463, 45

Méndez, A. & Rivera-Valentín, E. G. 2017, *ApJ*, 837, L1

Mizuno, H. 1980, *Progress of Theoretical Physics*, 64, 544

Mizuno, H., Nakazawa, K., & Hayashi, C. 1978, *Progress of Theoretical Physics*, 60, 699

Moldenhauer, T. W., Kuiper, R., Kley, W., & Ormel, C. W. 2021, *Astronomy and Astrophysics*, 646, 1

Mordasini, C., Alibert, Y., Benz, W., & Naef, D. 2009, *Astronomy and Astrophysics*, 501, 1161

Mordasini, C., Alibert, Y., Georgy, C., et al. 2012, *A&A*, 547, A112

Mordasini, C., van Boekel, R., Mollière, P., Henning, T., & Benneke, B. 2016, *ApJ*, 832, 41

Naoz, S., Farr, W. M., & Rasio, F. A. 2012, *ApJ*, 754, L36

Owen, J. E. & Lai, D. 2018, *MNRAS*, 479, 5012

Panichi, F., Goździewski, K., Migaszewski, C., & Szuszkiewicz, E. 2018, *MNRAS*, 478, 2480

Paredes, L. A., Henry, T. J., Quinn, S. N., et al. 2021, *AJ*, 162, 176

Pedregosa, F., Varoquaux, G., Gramfort, A., et al. 2011, *Journal of Machine Learning Research*, 12, 2825

Pepper, J., Rodriguez, J. E., Collins, K. A., et al. 2017, *AJ*, 153, 215

Perri, F. & Cameron, A. G. W. 1974, *Icarus*, 22, 416

Pollack, J. B., Hubickyj, O., Bodenheimer, P., et al. 1996, *Icarus*, 124, 62

Rafikov, R. R. 2006, *ApJ*, 648, 666

Rasio, F. A. & Ford, E. B. 1996, *Science*, 274, 954

Ribas, I., Reiners, A., Zechmeister, M., et al. 2023, *The CARMENES Search for Exoplanets around M Dwarfs. Guaranteed Time Observations Data Release 1 (2016-2020)*

Ricker, G. R., Vanderspek, R., Winn, J., et al. 2016, in *Proc. SPIE*, Vol. 9904, *Space Telescopes and Instrumentation 2016: Optical, Infrared, and Millimeter Wave*, 99042B

Rosenthal, L. J., Fulton, B. J., Hirsch, L. A., et al. 2021, *ApJS*, 255, 8

Sabotta, S., Schlecker, M., Chaturvedi, P., et al. 2021, *Astronomy & Astrophysics*, 653, A114

Schlecker, M., Burn, R., Sabotta, S., et al. 2022, *Astronomy & Astrophysics*, 664, A180

Schlecker, M., Kossakowski, D., Brahm, R., et al. 2020, *AJ*, 160, 275

Table 8: Radial velocity data obtained for TOI-899b.

BJD - 2450000	Radial Velocity (m/s)	Bisector (m/s)
<b>FEROS</b>		
8543.64921	44723.7 $\pm$ 8.7	-4.0 $\pm$ 12.0
8546.65455	44692.3 $\pm$ 10.7	-1.0 $\pm$ 15.0
8549.64390	44679.2 $\pm$ 8.2	8.0 $\pm$ 12.0
8550.66827	44654.1 $\pm$ 8.5	-12.0 $\pm$ 12.0
8551.59780	44691.6 $\pm$ 9.5	-15.0 $\pm$ 13.0
8553.65940	44712.6 $\pm$ 13.1	40.0 $\pm$ 17.0
8554.65929	44726.9 $\pm$ 12.7	42.0 $\pm$ 17.0
8555.63065	44692.3 $\pm$ 8.4	0.0 $\pm$ 12.0
8556.67850	44699.7 $\pm$ 9.5	-7.0 $\pm$ 13.0
8558.55750	44685.1 $\pm$ 10.1	33.0 $\pm$ 14.0
8560.66050	44639.7 $\pm$ 8.8	-30.0 $\pm$ 12.0
8566.58573	44678.9 $\pm$ 8.1	16.0 $\pm$ 12.0
8567.59465	44678.1 $\pm$ 8.2	-32.0 $\pm$ 12.0
8571.64310	44723.8 $\pm$ 10.7	15.0 $\pm$ 15.0
8572.60896	44653.8 $\pm$ 10.6	7.0 $\pm$ 15.0
8574.58052	44665.1 $\pm$ 12.1	23.0 $\pm$ 16.0
8593.48862	44730.5 $\pm$ 11.3	-3.0 $\pm$ 15.0
8617.51392	44719.2 $\pm$ 7.7	-20.0 $\pm$ 11.0
8619.48691	44681.9 $\pm$ 9.0	0.0 $\pm$ 13.0
8623.46101	44665.8 $\pm$ 16.2	7.0 $\pm$ 20.0
8624.47143	44700.0 $\pm$ 12.8	33.0 $\pm$ 17.0
8592.58057	44689.6 $\pm$ 18.3	-23.0 $\pm$ 18.0
8599.50975	44696.3 $\pm$ 9.9	1.0 $\pm$ 14.0
8625.46358	44670.2 $\pm$ 10.9	-31.0 $\pm$ 15.0
8626.47120	44696.6 $\pm$ 10.2	-32.0 $\pm$ 14.0
8627.46390	44696.7 $\pm$ 8.4	-6.0 $\pm$ 12.0
8637.49093	44685.7 $\pm$ 7.4	4.0 $\pm$ 11.0
8638.46431	44718.8 $\pm$ 9.4	-13.0 $\pm$ 13.0
8640.45795	44703.0 $\pm$ 9.5	-13.0 $\pm$ 13.0
8641.47584	44700.3 $\pm$ 13.1	-128.0 $\pm$ 17.0
8642.47749	44737.6 $\pm$ 11.4	-55.0 $\pm$ 15.0
8642.47684	44737.6 $\pm$ 11.4	-55.0 $\pm$ 15.0
8643.46106	44699.1 $\pm$ 9.1	9.0 $\pm$ 13.0
8645.47877	44772.1 $\pm$ 12.0	7.0 $\pm$ 16.0
<b>HARPS</b>		
8836.75538	44730.1 $\pm$ 3.9	-9.0 $\pm$ 5.0
8840.82178	44706.7 $\pm$ 3.7	-1.0 $\pm$ 5.0
8851.72242	44726.2 $\pm$ 3.7	-12.0 $\pm$ 5.0
8854.72962	44680.5 $\pm$ 8.4	-35.0 $\pm$ 11.0
8876.71642	44732.5 $\pm$ 4.8	-3.0 $\pm$ 6.0
8881.68161	44696.1 $\pm$ 5.1	-5.0 $\pm$ 7.0
8885.61656	44725.6 $\pm$ 7.2	1.0 $\pm$ 9.0
8890.66515	44715.4 $\pm$ 4.8	-19.0 $\pm$ 6.0
8899.62785	44726.4 $\pm$ 4.5	-6.0 $\pm$ 6.0
<b>CHIRON</b>		
9181.80350	43294 $\pm$ 24	—
9181.35804	43323 $\pm$ 28	—
9184.77684	43328 $\pm$ 35	—
9212.68165	43308 $\pm$ 25	—
9213.69339	43256 $\pm$ 39	—
9230.69126	43302 $\pm$ 41	—

Southworth, J. 2011, MNRAS, 417, 2166  
 Speagle, J. S. 2020, MNRAS, 493, 3132  
 Spiegel, D. S. & Burrows, A. 2013, ApJ, 772, 76  
 Stassun, K. G., Oelkers, R. J., Paegert, M., et al. 2019, AJ, 158, 138  
 Stumpe, M. C., Smith, J. C., Van Cleve, J. E., et al. 2012, PASP, 124, 985  
 Suzuki, D., Bennett, D. P., Ida, S., et al. 2018, The Astrophysical Journal, 869, L34  
 Suzuki, D., Bennett, D. P., Sumi, T., et al. 2016, The Astrophysical Journal, 833, 145  
 Szulágyi, J., Morbidelli, A., Crida, A., & Masset, F. 2014, Astrophysical Journal, 782  
 Tayar, J., Claytor, Z. R., Huber, D., & van Saders, J. 2022, ApJ, 927, 31  
 Thorngren, D. P., Fortney, J. J., Murray-Clay, R. A., & Lopez, E. D. 2016, ApJ, 831, 64  
 Tokovinin, A. 2018, PASP, 130, 035002  
 Tokovinin, A., Fischer, D. A., Bonati, M., et al. 2013, PASP, 125, 1336  
 Trifonov, T., Brahm, R., Espinoza, N., et al. 2021, AJ, 162, 283  
 Trifonov, T., Brahm, R., Jordán, A., et al. 2023, AJ, 165, 179  
 Twicken, J. D., Catanzarite, J. H., Clarke, B. D., et al. 2018, PASP, 130, 064502  
 van der Walt, S., Schönberger, J. L., Nunez-Iglesias, J., et al. 2014, PeerJ, 2, e453  
 Van Eylen, V., Dai, F., Mathur, S., et al. 2018, MNRAS, 478, 4866  
 Wakeford, H. R., Sing, D. K., Deming, D., et al. 2018, AJ, 155, 29  
 Welsh, W. F., Orosz, J. A., Carter, J. A., et al. 2012, Nature, 481, 475  
 Wong, I., Benneke, B., Gao, P., et al. 2020, AJ, 159, 234  
 Wu, Y. & Murray, N. 2003, ApJ, 589, 605  
 Yu, L., Rodriguez, J. E., Eastman, J. D., et al. 2018, AJ, 156, 127  
 Zhou, G., Bakos, G. Á., Bayliss, D., et al. 2019, AJ, 157, 31  
 Zhou, G., Quinn, S. N., Irwin, J., et al. 2021, AJ, 161, 2  
 Ziegler, C., Tokovinin, A., Briceño, C., et al. 2020, AJ, 159, 19

<sup>1</sup> Instituto de Astrofísica, Facultad de Física, Pontificia Universidad Católica de Chile, Av. Vicuña Mackenna 4860, Santiago, Chile.  
 e-mail: [firojas@uc.cl](mailto:firojas@uc.cl)

<sup>2</sup> Millennium Institute of Astrophysics, Santiago, Chile.

<sup>3</sup> Facultad de Ingeniería y Ciencias, Universidad Adolfo Ibáñez, Av. Diagonal las Torres 2640, Peñalolén, Santiago, Chile

<sup>4</sup> Data Observatory Foundation, Chile

<sup>5</sup> Space Telescope Science Institute, 3700 San Martin Drive, Baltimore, MD 21218, USA

<sup>6</sup> Max-Planck-Institut für Astronomie, Königstuhl 17, 69117 Heidelberg, Germany

<sup>7</sup> Observatoire de Genève, Département d’Astronomie, Université de Genève, Chemin Pegasi 51, 1290 Versoix, Switzerland

<sup>8</sup> Steward Observatory and Department of Astronomy, The University of Arizona, Tucson, AZ 85721, USA

<sup>9</sup> Department of Astronomy, Sofia University “St Kliment Ohridski”, 5 James Bourchier Blvd, BG-1164 Sofia, Bulgaria

<sup>10</sup> Landessternwarte, Zentrum für Astronomie der Universität Heidelberg, Königstuhl 12, D-69117 Heidelberg, Germany

<sup>11</sup> Department of Astrophysical Sciences, Princeton University, 4 Ivy Lane, Princeton, NJ 08544, USA

<sup>12</sup> INCT, Universidad de Atacama, calle Copayapu 485, Copiapo, Atacama, Chile

<sup>13</sup> Department of Physics and Kavli Institute for Astrophysics and Space Research, Massachusetts Institute of Technology, Cambridge, MA 02139, USA

<sup>14</sup> Earth and Planets Laboratory, Carnegie Institution for Science, 5241 Broad Branch Road, NW, Washington, DC 20015, USA

<sup>15</sup> Instituto de Astrofísica de Canarias (IAC), Calle Vía Láctea s/n, 38200, La Laguna, Tenerife, Spain

<sup>16</sup> Departamento de Astrofísica, Universidad de La Laguna (ULL), 38206 La Laguna, Tenerife, Spain

<sup>17</sup> Center for Astrophysics | Harvard & Smithsonian, 60 Garden St, Cambridge, MA 02138, USA

<sup>18</sup> Department of Earth, Atmospheric and Planetary Sciences, Massachusetts Institute of Technology, Cambridge, MA 02139, USA

<sup>19</sup> Astrobiology Research Unit, Université de Liège, 19C Allée du 6 Août, 4000 Liège, Belgium

<sup>20</sup> Kotizarovci Observatory, Sarsoni 90, 51216 Viskovo, Croatia

<sup>21</sup> South African Astronomical Observatory, P.O. Box 9, Observatory, Cape Town 7935, South Africa

<sup>22</sup> Université Côte d'Azur, Observatoire de la Côte d'Azur, CNRS, Laboratoire Lagrange, Bd de l'Observatoire, CS 34229, 06304 Nice cedex 4, France

<sup>23</sup> Observatories of the Carnegie Institution for Science, 813 Santa Barbara Street, Pasadena, CA 91101

<sup>24</sup> El Sauce Observatory, Coquimbo Province, Chile

<sup>25</sup> University of Southern Queensland, Centre for Astrophysics, West Street, Toowoomba, QLD 4350 Australia

<sup>26</sup> European Southern Observatory (ESO), Alonso de Córdova 3107, Vitacura, Casilla 19001, Santiago de Chile

<sup>27</sup> NASA Ames Research Center, Moffett Field, CA 94035, USA

<sup>28</sup> Department of Physics and Astronomy, The University of North Carolina at Chapel Hill, Chapel Hill, NC 27599, USA

<sup>29</sup> Instituto de Astronomía, Universidad Católica del Norte, Angamos 0610, 1270709 Antofagasta, Chile

<sup>30</sup> Physikalisches Institut, University of Bern, Gesellschaftstrasse 6, 3012 Bern, Switzerland

<sup>31</sup> Department of Earth, Atmospheric and Planetary Sciences, Massachusetts Institute of Technology, Cambridge, MA 02139, USA

<sup>32</sup> Department of Aeronautics and Astronautics, MIT, 77 Massachusetts Avenue, Cambridge, MA 02139, USA

<sup>33</sup> SETI Institute, Mountain View, CA 94043 USA

<sup>34</sup> Department of Astronomy, Tsinghua University, Beijing 100084, China

<sup>35</sup> Department of Physics, Engineering and Astronomy, Stephen F. Austin State University, 1936 North Street, Nacogdoches, TX 75962

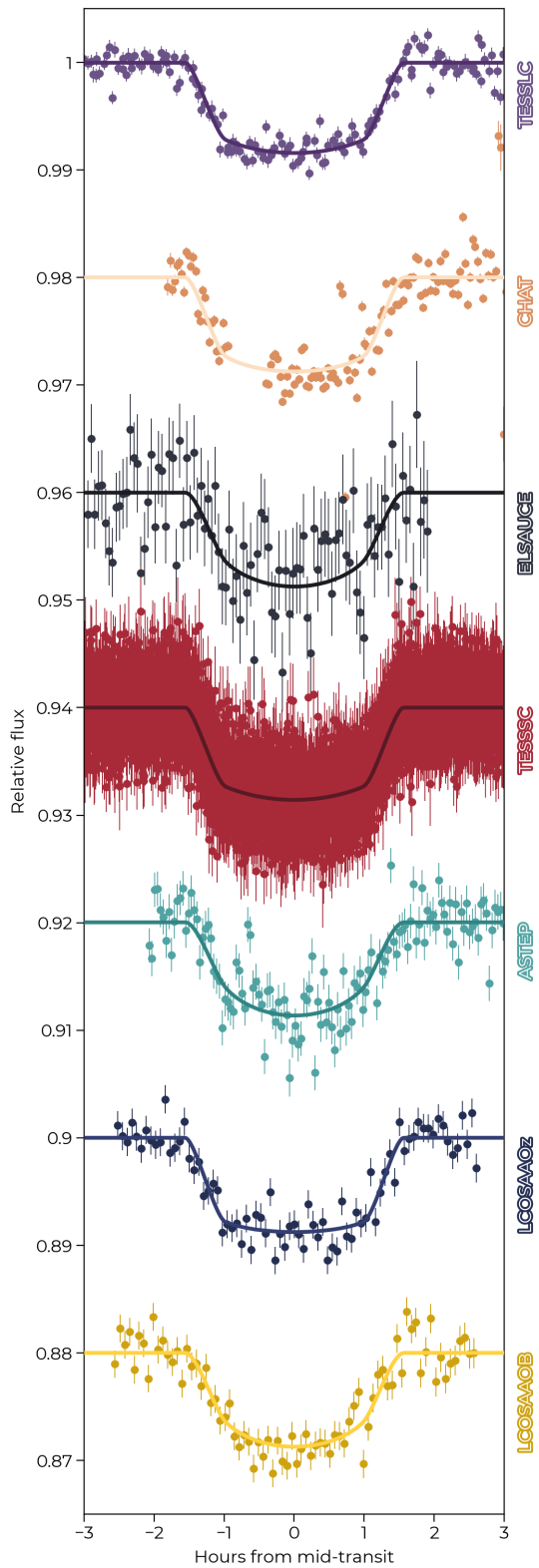


Fig. 10: Transit data observed for TOI-899b. The phase folded transit is plotted for both TESS long and short cadence. For CHAT and El Sauce, a single transit event is plotted.

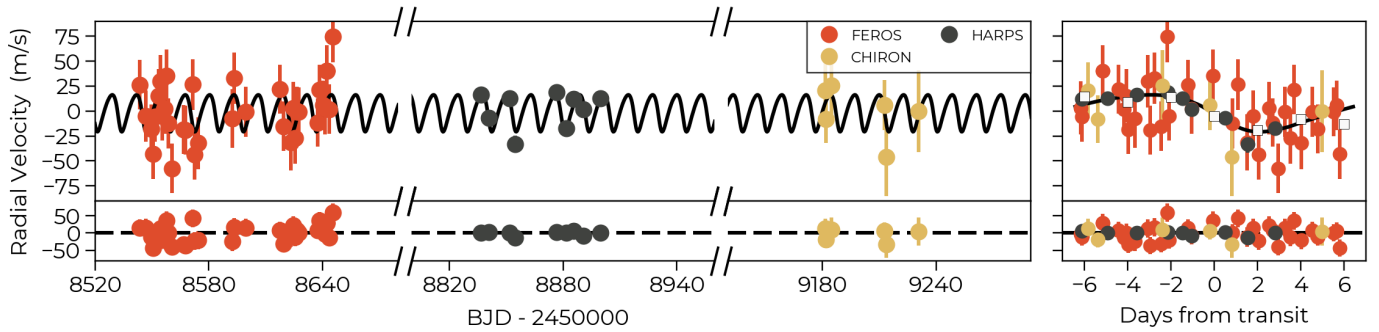


Fig. 11: Radial velocities from FEROS (orange-red), HARPS (black) and CHIRON (yellow) observed for TOI-899. The best Keplerian model is plotted as a black curve in both panels.

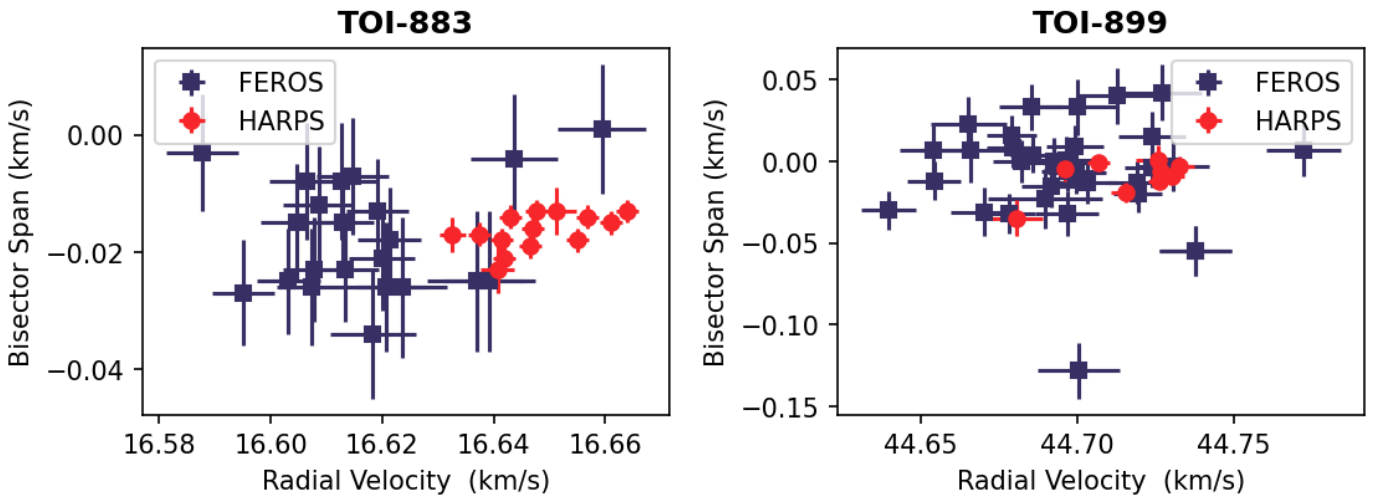


Fig. 12: Radial velocity data against the corresponding bisector span measured for each observation. No correlation was found between both targets.

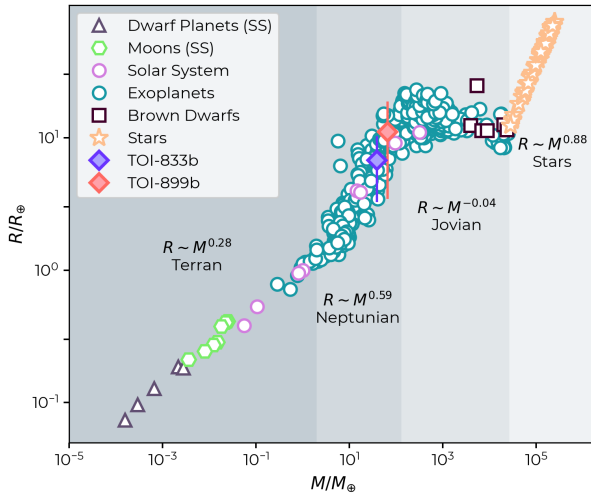


Fig. 13: Mass vs Radius diagram featuring the classification developed by [Chen & Kipping \(2017\)](#). Both targets are located close to the transition between Neptunian and Jovian planets. Exoplanet data are taken from the TEPCat catalog ([Southworth 2011](#)).

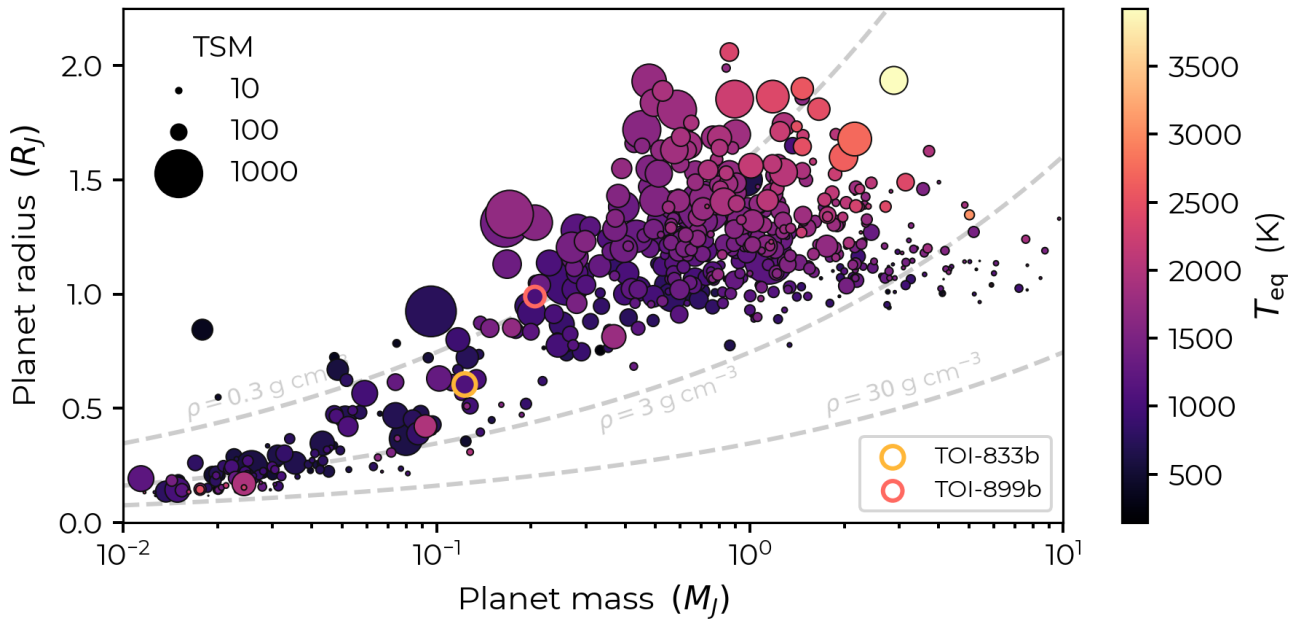


Fig. 14: Mass vs Radius diagram of well-characterized transiting planets (Southworth 2011). TOI-883b and TOI-899b are highlighted in yellow and red, respectively. Dot size scales with the Transmission Spectroscopy Metric (TSM) defined by Kempton et al. (2018b).

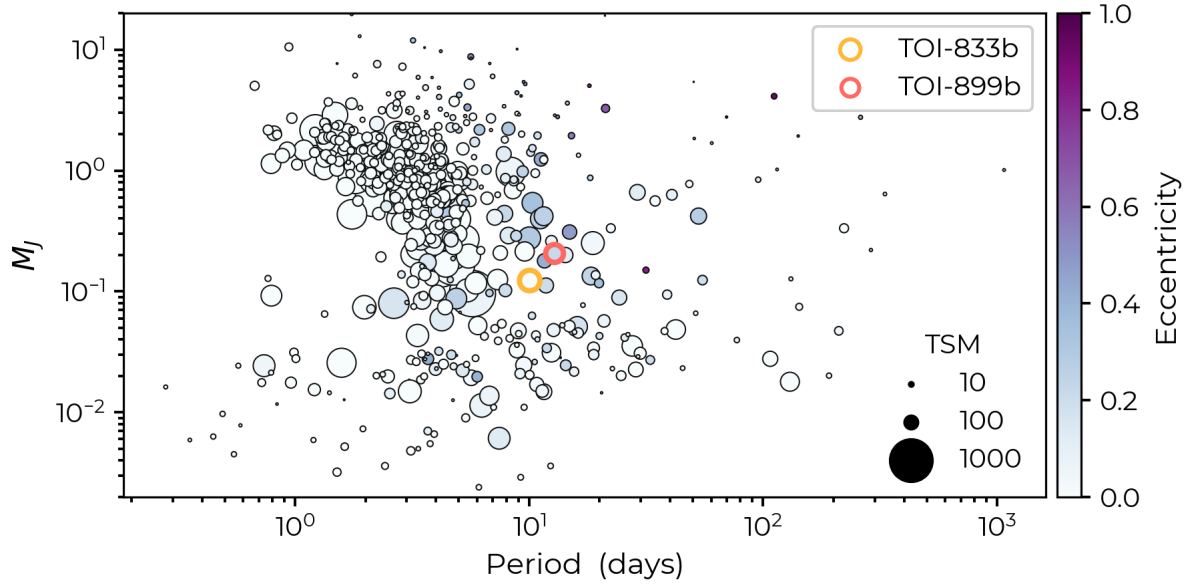


Fig. 15: Mass vs period diagram. This includes the TSM metric to compare against other similar Warm Giants. Eccentricity is also included, showing a noticeable contrast between the Warm Jupiter (some eccentric) and Hot Jupiter (mostly circular) populations.